Full title: Evidence for two distinct thalamocortical circuits in retrosplenial cortex

Abbreviated title: Two retrosplenial cortex subcircuits

Authors: Eleonora Lomi[1*], Mathias L. Mathiasen[2], Han Yin Cheng[3], Ningyu Zhang[4], John P. Aggleton[2], Anna S. Mitchell[1], Kate J. Jeffery[5]

1 – Department of Experimental Psychology, University of Oxford, The Tinsley Building, Mansfield Road, Oxford OX1 3SR, United Kingdom

2 - School of Psychology, Cardiff University, Cardiff, UK

3 - Department of Psychological and Brain Sciences, Dartmouth College, Hanover, New Hampshire, USA

4 - Institute of Neuroscience, State Key Laboratory of Neuroscience, CAS Center for Excellence in Brain Science and Intelligence Technology, Chinese Academy of Sciences, Shanghai 200031, China.

5 - Institute of Behavioural Neuroscience, Division of Psychology and Language Sciences, University College London, London WC1E 6BT, UK

*Corresponding author – Eleonora Lomi, email address: eleonora.lomi@some.ox.ac.uk

Abstract

Retrosplenial cortex (RSC) lies at the interface between perceptual and memory networks in the brain and mediates between these, although it is not yet known how. It has two distinct subregions, granular (gRSC) and dysgranular (dRSC). The present study investigated how these subregions differ with respect to their electrophysiology and connections, as a step towards understanding their functions. gRSC is more closely connected to the hippocampal system, in which theta-band local field potential oscillations are prominent. We therefore compared theta-rhythmic single-unit activity between the two RSC subregions and found, mostly in gRSC, a subpopulation of non-directional cells with spiking activity strongly entrained by theta oscillations, suggesting a stronger coupling of gRSC to the hippocampal system. We then used retrograde tracers to examine whether differences in neural coding between RSC subregions might reflect differential inputs from the anterior thalamus, which is a prominent source of RSC afferents. We found that gRSC and dRSC differ in their afferents from two AV subfields: dorsomedial (AVDM) and ventrolateral (AVVL). AVVL targets both gRSC and dRSC, while AVDM provides a selective projection to gRSC. These combined results suggest the existence of two distinct but interacting RSC subcircuits: one connecting AVDM to gRSC that may comprise part of the cognitive hippocampal system, and the other connecting AVVL to both RSC regions that may link hippocampal and perceptual regions. We suggest that these subcircuits are distinct to allow for differential weighting during integration of converging sensory and cognitive computations: an integration that may take place in thalamus, RSC or both.

Keywords

Retrosplenial cortex, anterior thalamus, thalamocortical, theta-modulation, spatial memory, chronic rodent electrophysiology.

Highlights

- The two retrosplenial cortex subregions, gRSC and dRSC, differ in their temporal firing characteristics and relation to theta oscillations.
- There are differential afferents from the anteroventral thalamic nucleus to gRSC and dRSC, with the dorsomedial subnucleus projecting selectively to gRSC.
- The anteroventral thalamus-retrosplenial cortex circuitry thus comprises two functionally and anatomically distinct but connected circuits, differentially connected to the hippocampal system, that may support the integration of cognitive and perceptual information.

57 # 1.0 Introduction

58 Retrosplenial cortex is a brain region lying between primary sensory cortices and the
59 hippocampal spatial memory system. It has two component subregions, granular (gRSC) and
60 dysgranular (dRSC), that may serve different, albeit related, functions (Aggleton et al., this
61 issue). In order to shed light on these functions we first explored how gRSC and dRSC differ
62 electrophysiologically and then traced the thalamic afferents, which form some of the most
63 prominent inputs to RSC, to try and shed light on what may account for these differences.

64 Retrosplenial cortex (RSC) is a fundamental component of an extended hippocampal circuit
65 supporting learning and memory (Vann et al., 2009). The hippocampus, RSC and anterior
66 thalamus (ATN) also comprise core brain areas linked to neurodegeneration in Alzheimer's
67 disease (Braak and Braak, 1991; Raji et al., 2009). Spatial memory is a prominent component
68 of this system: selective RSC damage in humans or animals results in memory deficits and
69 also spatial disorientation (Reed and Squire, 1997; Sutherland and Hoesing, 1993; Vann and
70 Aggleton, 2002, 2004, 2005; Whishaw et al., 2001; Pothuizen et al., 2008, 2009, 2010;
71 Aggleton et al., 1995; Cooper and Mizumori, 1999, 2001). Human functional imaging studies
72 provide further evidence of the spatial functions attributed to the RSC (Maguire, 2001; Auger
73 et al., 2012). While rodent studies have also characterized the spatial functions of the RSC
74 (Vann et al., 2009) the details are far from complete (Mitchell et al., 2018), although
75 directional processing is a prominent feature (Cho and Sharp, 2001; Lozano et al., 2017;
76 Alexander et al., 2020; Chen at al., 1994).

77 The topography of connections of each of the major RSC subregions, gRSC and dRSC,
78 represents a key aspect for functional considerations on the RSC involvement in navigation

and memory (Vann et al., 2009). While the RSC has critical connections with three main areas, the hippocampal formation, ATN, and visuospatial neocortical areas, these connections are not equally shared between the two RSC subregions (van Groen and Wyss, 1990, 1990b, 1992; Van Groen and Wyss, 2003; Vogt and Miller, 1983; Cenquizca and Swanson, 2007; Sripanidkulchai and Wyss, 1986; Sugar et al., 2011). gRSC connectivity is strongly coupled with regions of the hippocampal formation that are involved in spatial navigation and memory processes, as it receives direct inputs from the dorsal hippocampus, primarily from subiculum (Meibach and Siegel, 1977; Yamawaki et al., 2019; Opalka et al., 2020), and secondarily from CA1, both glutamatergic (Haugland et al., 2019; van Groen and Wyss, 1990) and GABAergic (Opalka et al., 2020; Unal et al., 2015; Jinno et al., 2007). In contrast, dRSC does not receive direct CA1 inputs and receives only sparse subicular inputs (van Groen and Wyss, 1990b, 1992; Vogt and Miller, 1983; Witter et al., 1990).

The gRSC also receives extensive inputs from basal forebrain structures that are involved in the generation of hippocampal theta (6-12Hz) oscillations. These regions are the medial septum, and diagonal and horizontal band of Broca (Unal et al., 2015; Van Groen and Wyss, 2003). Across these regions, theta oscillations are clearly present in the local field potential (LFP) and are believed to reflect the relaying of information (perhaps timing) related to hippocampal function (Burgess et al., 2002; Buzsáki, 2002, 2005; Hasselmo and Eichenbaum, 2005). By contrast, instead of these limbic inputs, dRSC is characterized by stronger connections directly from primary/secondary visual cortices and laterodorsal/ lateroposterior thalamus (van Groen and Wyss, 1990, 1990b, 1992), which are considered to endow dRSC with a privileged role in visuospatial processing (Vann & Aggleton, 2005). Jacob et al. (2017) extended this idea by showing a functional difference in the electrophysiological recordings

102 between RSC subregions in rats. While global head direction encoding was present in both
103 gRSC and dRSC, a directional signal more sensitive to local visual landmarks was found only
104 in dRSC (Jacob et al., 2017). Conjunctive head direction and landmark coding in dRSC has
105 been accounted for by reference to its stronger visual inputs as compared to global directional
106 inputs ascending from the ATN (Page and Jeffery, 2018; Fischer et al., 2020).

107 Within the ATN, the anterodorsal (AD) and anteroventral (AV) nuclei are reciprocally
108 interconnected to the two RSC subregions, although both appear to have a stronger
109 relationship with the granular compared to the dysgranular part (Witter et al., 1990; Shibata,
110 1993, 1994; Van Groen and Wyss, 1995). While 56% of AD neurons are head direction cells
111 (Taube, 1995; Taube, 2007; Clark and Taube, 2012), the majority of AV neurons (75%) have
112 firing entrained by the theta oscillations (Vertes et al., 2001; Albo et al., 2003; Tsanov et al.,
113 2010, 2011), suggesting that two main information streams, head direction vs theta, ascend
114 through the ATN, with a parallel organization (AD vs AV). Given that theta propagation is
115 thought to serve spatial mnemonic functions of the limbic system by optimizing synaptic
116 plasticity and inter-regional communication (Hyman et al., 2003; Buzsáki, 2002, 2005;
117 Buzsáki and Moser, 2013), we used theta as a marker for hippocampal coupling to determine
118 whether gRSC and dRSC have distinct interactions with hippocampus. We hypothesized that
119 theta-rhythmic firing would be stronger in gRSC compared to dRSC, reflecting a stronger
120 interaction with the hippocampal navigational network. We then used retrograde tracing to see
121 if the anterior thalamic inputs to the two subregions could be differentiated. As we show here,
122 we found that gRSC is more theta-modulated than dRSC, and with anatomical tracing we then
123 found that it selectively receives a stronger input from dorsomedial AV (AVDM). These
124 findings strengthen the evidence that gRSC is part of a subcircuit that connects with the

125 hippocampal system, while dRSC is a parallel circuit that interacts more strongly with sensory
126 cortices. We finish with some speculations about a possible role for RSC in linking these two
127 systems.

128 2.0 Methods and Materials

129 2.1 Electrophysiology recording experiment

130 2.1.1 Animals and coordinates

131 For this study we used data from four male Lister Hooded rats (Charles River, UK) that were
132 surgically implanted with tetrodes. Two of the rats (R602, R636) had participated in a
133 previously published experiment (Jacob et al., 2017) and two were part of a new experiment
134 (Zhang et al., in prep). We only included rats in which we could identify the electrode track in
135 the histological section, and for which histology indicated that electrodes sampled both RSC
136 subregions (electrodes advanced from dRSC into gRSC).

137 Surgery followed standard stereotaxic surgery techniques for chronic recording of
138 extra-cellular activity in behaving animals (Szymusiak and Nitz, 2003). Implant coordinates
139 were based on previous study of head direction cells in the RSC of Jacob et al. (2017). These
140 were as follows: AP, -5.5; -5.8; ML, ±1.0 - ±0.80; DV, 0.4 - 0.65 (in mm from Bregma). All rats
141 were implanted in the left hemisphere. All experiments were carried out in accordance with
142 UK Animals (Scientific Procedures) Act, 1986 and EU directive (2010/63/EU), complying
143 with ARRIVE guidelines for the care and use of laboratory animals.

2.1.2 Behavioral protocol and testing apparatus

Animals were screened daily for single unit activity. Screenings were made in an open field box in within a cue-rich room. When a set of units was isolated, the animal was transferred to the experimental room and the recording session was conducted in a two-compartment box, which was configured to test a hypothesis (not addressed here) about directional encoding. Briefly, the apparatus comprised two identical rectangular compartments connected by a central doorway in the long wall that separated them (for details see Jacob et al., 2017). One short wall of each compartment was adorned with a large white cue card, and the compartments were differentially scented, one with lemon and one with vanilla. The apparatus was located within a curtained-off area. Each recording session consisted of five consecutive trials, with each trial involving a different box orientation. To promote exploratory behavior throughout the recording, rice was randomly thrown in the box by the experimenter. For the purposes of the present analysis, only the first 10min-long baseline trial was considered.

2.1.3 Signal processing and tracking

Single unit and LFP signals were recorded using a headstage amplifier connected to a microdrive and connected to the multichannel recording system (DacqUSB, Axona) via a flexible lightweight cable. Single unit activity was continuously sampled (48 kHz sampling frequency), amplified 15-50K times and band-pass filtered from 300 Hz to 7 kHz. The signal from each electrode was differentially recorded against the signal from an electrode on a different tetrode with low spiking activity. Spikes were defined as short-lasting events exceeding a user-defined voltage threshold. Spikes were time- stamped and stored together

166 with a 1ms of surrounding signal (with 200 µs pre- and 800 µs post-threshold interval).
167 Tetrodes were lowered by 25-150 µm to locate single-unit spiking activity. The LFP signal
168 was collected single-ended (250 Hz sampling frequency), amplified 5k times, filtered with a
169 500 Hz low-pass filter and stored with the unit data. A 50 Hz notch filter was applied to
170 remove local mains noise. Two light-emitting diodes (LEDs), one large and one small and
171 separated by 5 cm, were attached to the headstage to provide the position and the orientation
172 of the rat's head. The LEDs were imaged with an overhead camera (50 Hz sampling rate).
173 Spike times, LFP signal, position in x- and y-coordinates and directional heading in
174 degrees were saved for offline analysis.

175 **2.1.4 Data analysis**

176 Data were analyzed using TINT (Axona, UK) and MATLAB R2018a (MathWorks, USA)
177 with custom-made programs and functions. CircStat toolbox was used for analysis using
178 circular statistics (Berens, 2009).

179 **2.1.5 Spike sorting**

180 Spike-sorting was performed using KlustaKwik (Kadir et al., 2014) followed by manual
181 refinement using the TINT software package (Axona). To confirm that isolated clusters
182 resulted from single unit activity, the following inclusion criteria were adopted: (1) an average
183 waveform displaying the classical action potential shape, and (2) fewer than 10% of spikes
184 occurring in the first 2ms of the autocorrelogram (action potential refractory period). Only
185 cells meeting these criteria were accepted into further analysis.

186 **2.1.6 Spectral analysis**

187 The LFP signal, recorded by low-pass filtering the raw neural signal, was analyzed using a
188 fast Fourier transform (FFT). The power of each frequency component was defined as the
189 square of the magnitude of the output of the FFT. To compare across animals, power
190 measures within each trial were normalized to z-scores and then plotted and smoothed with a
191 Gaussian kernel (bandwidth = 2Hz; standard deviation = 0.5Hz). The power of theta
192 frequency was found as the maximum z-score within the movement-associated (Type-1) theta
193 frequency range (6-12Hz). Average theta frequency was found as the frequency value
194 associated to peak theta power.

195 **2.1.7 Theta analysis**

196 To investigate spike-LFP coupling, the LFP signal was filtered offline for Type-1 theta using
197 a 4th order Butterworth filter with band-pass between 6-12Hz. A zero-phase filtering was
198 applied to prevent the phase shift introduced by the Butterworth filter. The Hilbert transform
199 was then applied to the bandpass-filtered LFP to derive instantaneous theta phases (250Hz
200 sampling rate). Each theta cycle was defined such that peaks occurred at 0° and 360°, with a
201 trough at 180°. To determine at which point to apply the Hilbert Transform, the LFP signal
202 (Hz) was linearly interpolated with spike time (s), with each spike being assigned to the phase
203 of the theta cycle at which it occurred. To visualize the spike-LFP relationship, we then
204 double-plotted a spike-phase histogram for each cell. The probability distribution of spikes
205 relative to theta phases was derived by smoothing the spike-phase histogram using a circular
206 kernel density estimation (KDE) method, with an automatically selected bandwidth parameter
207 using the plug-in rule of Taylor (2008).

208 Theta spike-LFP coherence and rhythmicity were assessed by computing an index of theta
209 phase-coupling (IC) and an index of rhythmicity (IR), respectively. Coupling refers to the
210 phase of theta at which spikes occurred, as spikes may be emitted with a timing coupled to
211 theta (phase-locked) even if there is no overt rhythmicity on the autocorrelogram (Eliav et al.,
212 2018). We computed an IC by computing the mean vector length (Rayleigh vector, CircStat
213 toolbox) of the spikes vs theta phase distribution (Climer et al., 2015; Frank et al., 2001). For
214 each cell, spike phases were binned between 0 and 360° with 6° bins. For each cell with IC >
215 99th percentile of shuffle distribution, the preferred theta phase was estimated as the circular
216 mean of all the spike phases, and a Rayleigh test was conducted to assess the significance of
217 this phase preference across cells (see Supplementary materials, Section 1.2). This value was
218 used to sort cells into theta-modulated vs. not.

219 The IR additionally quantifies the temporal modulation of a cell's firing at theta frequency
220 range (6-12Hz). A theta-rhythmic cell will show peaks at ~125ms on its autocorrelogram.
221 Autocorrelograms of the spike trains were plotted between ± 500ms using 10ms bins,
222 normalized to the maximum value and smoothed (20 bins boxcar). Following methods
223 outlined in Lozano et al. (2017), the IR was calculated as the difference between the expected
224 theta modulation-trough (autocorrelogram value between 60-70ms) and the theta-modulation
225 peak (autocorrelogram value between 120-130ms), divided by their sum. It takes values
226 between -1 and 1.

227 **2.1.8 Cell identification and inclusion criteria**

228 Head direction and bidirectional cells were identified as described in Jacob et al. (2017), and
229 removed from the current analysis, as they were previously included in Jacob et al. (2017),

and they were not theta-modulated. Briefly, to analyze the directional firing characteristics of single units, the spike times and position samples of the rat's facing direction were sorted into bins of 6°. The mean firing rates per angular bin (Hz) were smoothed with a 5-bin (30°) smoothing kernel and polar-plotted. Finally, the angles were doubled and plotted modulo 360° in order to remove any bidirectionality that might be present in the tuning curves of bidirectionally tuned cells.

To be considered for analysis, cells needed to have (1) a tuning curve that was not obviously unimodal/bidirectional from visual inspection; (2) Rayleigh vector length of the doubled head direction angles < 0.22, which is the original threshold used by Jacob et al. (2017) and (3) average firing rate > 0.1Hz for the trial.

To provide a control for each cell against which to measure its theta-phase coupling we created a time-shifted null distribution in which the entire sequence of spike times was circularly time-shifted by a random amount lying between 20s and the duration of the recording session minus 20s. This preserved the number of spikes and the temporal structure of the spiking sequence, but dissociated the time of spiking from the theta oscillations. This was repeated 1000 times for each cell, and the IC was computed for each repetition. All values were pooled together to derive a control distribution, representing the chance level for which the activity of each RSC cell was locked to theta. A cell was considered as significantly modulated at theta frequency if the IC was >99th percentile of the control distribution for that neuron.

250 **2.1.9 Cell-specific temporal firing characteristics**

251 To investigate bursting properties of RSC neurons, inter-spike intervals (ISI) were plotted in a
252 frequency histogram between 0-250ms. Cells with peak ISI <10ms, which defines a burst
253 mode (Fanselow et al., 2001), were classified as bursting and the remainder as tonic. The
254 burst index was calculated as the ratio of spikes with peak ISI <10ms to all the spikes in a trial
255 (Mizuseki et al., 2012). Burst index values closer to 1 indicate the presence of intra-burst
256 spikes, whereas smaller values indicate a prevalence of single spikes.

257 **2.1.10 Waveform analysis**

258 Peak-to-trough waveform width was used to separate narrow from broad spiking cell types
259 (Lewicki, 1998). We followed methods reported in Ardid et al. (2015), using the open source
260 code from the public Git repository: https://bitbucket.org/sardid/waveformanalysis
261 (Waveform Analysis toolbox; Ardid et al., 2015). Briefly, a two-Gaussian model was applied
262 to the distribution of waveform widths. We defined two cutoffs on this model that divided
263 waveforms into three groups: narrow, broad and in-between. Broad waveforms were those for
264 which the likelihood to be considered broad was larger than 10 times the likelihood to be
265 narrow. Narrow waveforms were those for which the likelihood to be considered narrow was
266 larger than 10 times the likelihood to be broad. Unclassified waveforms were those falling
267 into the dip of the bimodal distribution. The bimodality of the distribution was tested using
268 the calibrated version of the Hartigan dip test ($p < 0.01$).

269 **2.1.11 Statistics**

270 For gRSC-dRSC comparisons, if data were found to deviate significantly from a normal
271 distribution (Matlab functions *kstest*), we used a non-parametric test (Wilcoxon Rank-sum

272 test, WRS, Matlab function *ranksum*). Otherwise, we used parametric tests. To evaluate
273 simultaneously the effect of two grouping variables (brain region and cell type) on waveform
274 parameters, we used a two-way ANOVA. We also used the Chi-squared goodness-of-fit test
275 (X^2) when testing observed numbers of theta-rhythmic cells in gRSC and dRSC against an
276 expected equal proportion, and the number of interneurons against an expected equal
277 proportion. To test the significance between two circular distributions, we employed the
278 Watson-Williams multi-sample F-test for equal circular means (WW, Matlab function
279 *circ_wwtest*, Circular statistics toolbox), in addition to the Rayleigh test. All statistical tests
280 are two-tailed. For all box plots, a line is marked at the sample median, boxes at the
281 interquartile range, whiskers at the minimum and maximum value. Markers represent
282 individual data points. In all figures and tables, p-value significance level: $*$ = 0.05, $**$ = 0.01,
283 $***$ = 0.001.

284 **2.2 Retrograde tracer experiment**

285 **2.2.1 Animals and tracers**

286 Twenty-three male Lister hooded rats (Charles River, UK; Envigo, UK) weighing 291-614g at the
287 time of surgery were used for the retrograde tracer experiments. Four retrograde tracers were
288 employed for a total of 29 injections: (i) cholera toxin subunit B (CTB; Polysciences Inc,
289 Eppelheim, Germany), (ii) fast blue (FB; Polysciences Inc, Eppelheim, Germany), (iii) biotinylated
290 dextran amine tracer (BDA; 3 kD version; Life Technologies Ltd, Paisley, UK), and (iv)
291 fluorogold (FG; Fluorochrome Inc., Denver, CO, USA). The CTB was used either
292 unconjugated or conjugated with Alexa Fluor 594 (Ctb-AF594; Molecular Probes, Invitrogen
293 Inc.) or with Alexa Fluor 488 (Ctb-AF488; Molecular Probes, Invitrogen Inc.). The single

294 BDA case was also included in a previous study (Mathiasen et al., 2017), which provides full
295 methodological procedures for this tracer. Six animals had dual injections while the others had
296 single injections placed in either gRSC or dRSC.

297 **2.2.2 Surgery**

298 All injection surgeries took place under isoflurane anesthesia (isoflurane-oxygen mixture 1.5-
299 2.5%) with the rat positioned in a stereotaxic frame (Kopf Instruments, Tujunga, CA). A
300 dorsal craniotomy exposed the central sinus and adjacent tissue. Lambda and bregma were set
301 at the same depth coordinates, creating a flat skull. Tracers were injected either mechanically
302 (all FB, FG, Ctb-AF594, Ctb-AF488 injections) via a 0.5µl, 0.66µl or 1.0µl Hamilton pipette
303 (Hamilton, Bonaduz, Switzerland) or iontophoretically. See Supplementary materials **(Tables**
304 **3-4)** for injection coordinates. Mechanical tracer injections were infused with a flow of 10-20
305 nl/min. In all cases, the needle was left in place for a further 10min before being retracted. As
306 a part of the analgesia regime, Lidocaine was administered topically to the scalp (0.1ml of 20
307 mg/ml solution; B. Braun, Melsungen, Germany) and meloxicam was given subcutaneously
308 (0.06ml of 5mg/ml solution, Boehringer Ingelheim Ltd, Berkshire, UK). After 6-8 days post-
309 injection, each rat was perfused and histological analysis was performed (see section
310 Histology).

311 **2.3 Histology and tracing**

312 At the completion of all experiments, rats received an overdose of sodium pentobarbital
313 (Euthatal, Merial, Harlow, United Kingdom) and were perfused transcardially with 0.1 M
314 phosphate-buffered saline (PBS) followed by paraformaldehyde (PFA) perfusion (4%

315 paraformaldehyde solution in 0.1 M PBS) or with saline (0.9% sodium chloride solution)
316 followed by 10% formalin perfusion (10% formalin in 0.9% sodium chloride solution). The
317 brains were removed, stored in 10% formalin or PFA, followed by 25-30% sucrose solution (25-
318 30% in 0.1 M PBS), and finally frozen with dry ice. Sections were cut coronally (30-50µm) with
319 a freezing microtome or cryostat and were mounted on glass slides. Tetrode locations were
320 histologically verified from cresyl violet-stained brain section. Digital pictures were acquired
321 with an Olympus microscope (Olympus Keymed, Southend-on-Sea, U.K.)

322 In cases with unconjugated CTB tracer injections, sections were first washed for 3x10 min in 0.1 M
323 PBS, washed 3 x 10 min in PBS-TX (0.2% Triton X-100 in 0.1M PBS) and incubated with the
324 primary antibody rabbit anti-CTB overnight (1:3000) (Sigma-Aldrich, UK). Sections were washed
325 for 3 x 10 min (PBS-TX) and incubated with the secondary antibody goat anti-rabbit (1:200)
326 (conjugated to DyLight 594; Vector Laboratories, CA) for two hours. After a further 3 x 10 min
327 wash (PBS), sections were mounted. Sections were then further dehydrated (ethanol), defatted
328 (xylene), and coverslipped with DPX. All slides were mounted in DPX or Vectashield antifade
329 mounting medium (Vectorlab, H-1000). Slides from animal 717 were mounted in Vectashield
330 antifade mounting medium with propidium iodide (Vectorlab, H-1300) which stained the
331 nucleus red, while slides from animal 878 were mounted in Vectashield antifade mounting
332 medium with DAPI (Vectorlab, H-1200) which stained the nucleus blue. Slides were analysed
333 for retrograde cell labelling in the AV, using epi-fluorescence microscopy for CTB, FG and FB
334 labelling and brightfield microscopy for the single case with BDA label. For visualization
335 purposes, FG labelled images were pseudo-coloured in cyan, CTB and Ctb-AF594 in red, Ctb
336 -AF488 in green and FB in blue.

337

338 # 3.0 Results

339 ## 3.1 RSC electrophysiological experiment

340 ### 3.1.1 Histology

341 As mentioned earlier, for the analysis we only included four rats for which histology indicated
342 that electrodes sampled both RSC subregions (electrodes advanced from dRSC into gRSC).
343 For each electrode bundle, we marked on the relevant histological section our best estimate of
344 the electrode tip. The cell locations were estimated based on the reconstruction of the
345 electrode tract from histology and the record of screw turns that lowered the electrodes each
346 day, starting from a known DV within the dRSC. **Figure 1** illustrates examples of brain
347 sections in which the electrode track is clearly visible. For one animal (R887), the tract
348 suggested that electrodes were implanted more laterally and were advanced through the white
349 matter tract of the cingulum fibres (Cg; **Figure 1;** See Supplementary materials, **Section 1.1)**
350 and this could explain the under sampling of cells from this animal (see **Table 1,** first row).

351

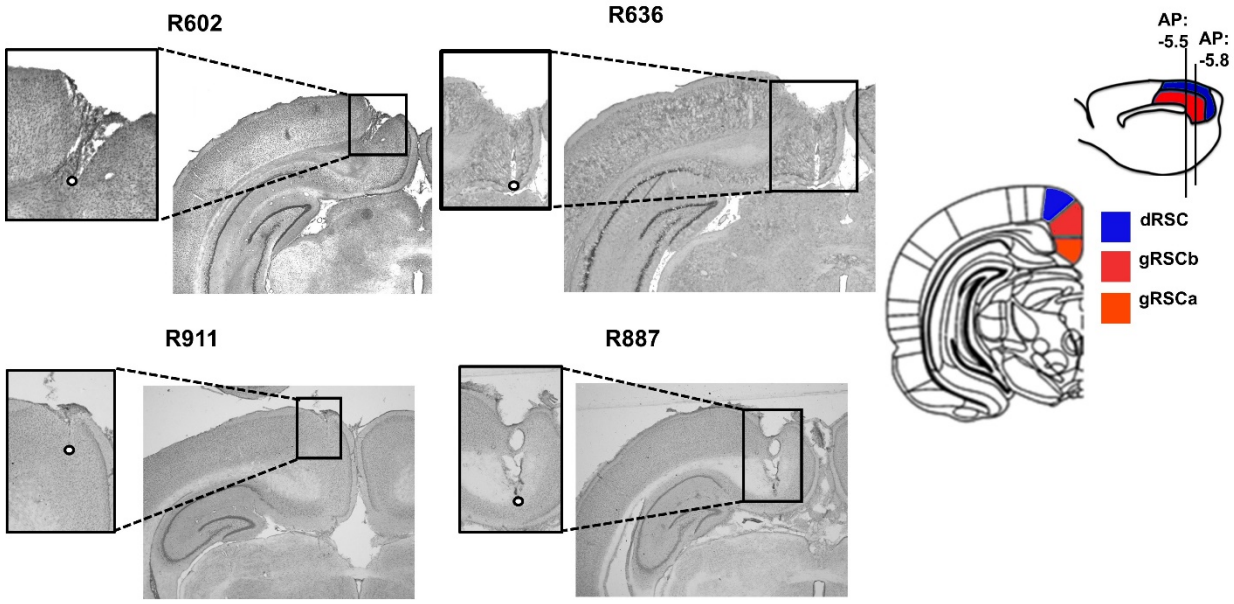

Figure 1. Histology of RSC recordings. Left: Photomicrographs of the Nissl-stained coronal sections through the recording site, for each of the four rats implanted in RSC (left hemisphere). White dots depict the final electrode depth. Top right: schematic of the AP-level (mm) of the recording sites within the RSC. R636 and R602, AP = -5.8; R911 and R887, AP = -5.5. AP-levels estimated based on the shape of cingulum fibers (Cg) and the width of the central sulcus (See supplementary materials, Section 1.1.). Middle right: schematic of the RSC subregions for a coronal AP level of -5.5, adapted from Paxinos and Watson (2007). Images for R602 and R636 were supplied by the authors of Jacob et al. (2017).

3.1.2 The same LFP theta oscillations are recorded from gRSC and dRSC.

Consistent with previous work in freely moving animals, the LFP showed characteristic network patterns, including clear theta oscillations (Dillingham et al., 2019; Young and McNaughton, 2009; Borst et al., 1987; Talk et al., 2004). Theta oscillations from gRSC and dRSC did not differ in average peak Type-1 (movement-associated; Olvera-Cortés et al., 2002; Caplan et al., 2003) theta power and frequency (6-12Hz; **Figure 2**). Average peak theta power was 6.88 ± 0.38 for gRSC recordings and 6.577 ± 0.35 for dRSC recordings (WRS test,

z = 0.7, p = 0.49). The associated average frequency was 8.73 ± 0.14Hz for gRSC recordings and 8.63 ± 0.16Hz for dRSC recordings (z = -0.84, p = 0.40). The lack of differences between gRSC and dRSC LFP was maintained when the data were segregated according to animal (WRS test, all $p > 0.05$).

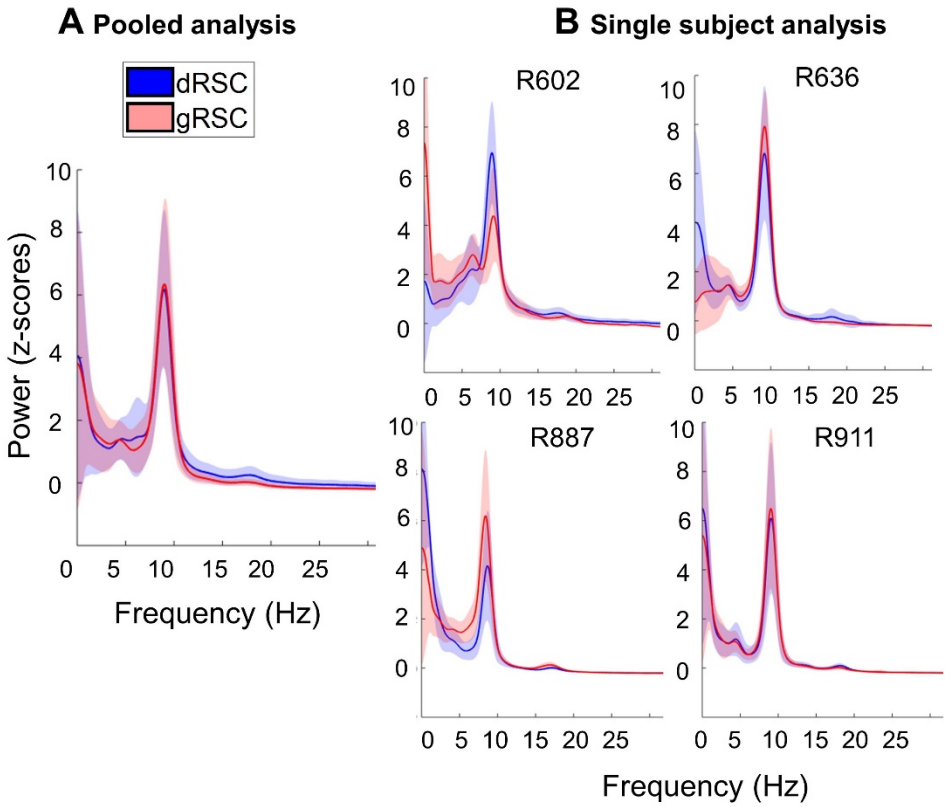

Figure 2. Theta oscillations have the same power and frequency. Average normalized power spectrum across all trials, **(A)** combined across all animals (n=4; pooled analysis), and **(B)** within each animal (single subject analysis). Shaded area is the standard deviation. X-axis, frequency (Hz); y-axis, power (z-scores). No difference in LFP theta oscillations were seen between gRSC and dRSC.

378 **3.1.3 An anatomically organized theta-modulated cell population exists in the RSC**

379 We then looked at theta-band properties of spiking in single neurons. A total of 642 non-
380 directional cells were analyzed from the four rats moving freely in the two-compartment box
381 to determine whether there is differential coupling of gRSC and dRSC with the hippocampal
382 navigational network, reflected in differential theta modulation. Single-cell results were
383 obtained first after pooling cells across animals into a single distribution (pooled analysis),
384 and second, from cells recorded for each animal individually (single subject analysis). Unless
385 otherwise stated, the same results were observed in both analyses and between animals.

386 We first assessed whether cells were theta-modulated by determining their IC. Of the 642
387 non-directional cells identified, 292 cells came from gRSC and 350 from dRSC. Of these
388 cells, half (n = 321/642, 50%) reached the criterion for significant theta modulation, based on
389 the IC being greater than 99th percentile of the control distribution for that neuron. **Table 1**
390 reports a summary of recording locations and number of theta-phase-locked cells recorded in
391 each RSC subregion for the four animals.

392 **Table 1.** Distribution and electrophysiological properties of non-directional RSC neurons.

393 Average for each animal and combined across animals, compared between gRSC and dRSC.

Non-directional neurons						
	Area	**R602**	**R636**	**R887**	**R911**	**All rats**
No. of trials		30	29	16	30	105
No. of non-directional theta-modulated cells	gRSC	41/64	79/105	10/15	66/108	196/292
	dRSC	86/265	7/24	13/18	19/43	125/350
	both	127/329	86/129	23/33	85/151	321/642
% of non-directional theta-modulated cells	gRSC	64%	75%	67%	61%	67%
	dRSC	32%***	29%***	72%	44%*	36%***
Mean rate (Hz)	gRSC	4.08	4.91	5.88	4.52	4.63 ± 0.5
	dRSC	3.39**	2.34***	4.54**	1.42***	3.13 ± 0.19**
Burst Index	gRSC	0.08	0.07	0.16	0.1	0.08 ± 0.007
	dRSC	0.04**	0.03**	0.04***	0.02**	0.04 ± 0.003 ***
Index of theta-phase coupling (IC)	gRSC	0.1	0.14	0.19	0.19	0.15 ± 0.008
	dRSC	0.06***	0.06***	0.07**	0.08***	0.06 ± 0.003 ***
Index of Rhythmicity (IR)	gRSC	0.0001	0.04	-0.01	0.06	0.04 ± 0.27
	dRSC	-0.01	-0.01*	-0.02	-0.05	-0.02 ± 0.22 ***
Peak-to-Trough width (μs)	gRSC	258.13	318.29	186.67	299.81	291.51 ± 9.26
	dRSC	359.32***	350	377.78*	373.95**	361.43 ± 7.39 ***

394 For each rat, the following are reported: total number of trials, number of theta-modulated cells/

395 number of cells, electrophysiological properties. Significance of differences in proportions was

396 tested using X^2 test for differences in expected proportions. Otherwise, multiple two-sample

397 WRS tests were used. The level of significance of each test is indicated for each animal and

398 across animals. The last column contains the results of the pooled analysis (average ± SEM). The
399 level of significance of each test is indicated for all within subjects and pooled comparisons.

400 Despite the lack of LFP theta differences between gRSC and dRSC recordings discussed
401 above, the distribution of theta-modulated cells varied considerably between RSC subregions,
402 as indicated by the significance of a X^2 test for differences in proportions. Across all animals,
403 67.1% (196/292) of gRSC cells fired in phase with theta, compared to only 35.7% (125/350)
404 of dRSC cells ($\chi^2 = 62.82$; $p < 0.0001$). Significant differences were confirmed when the data
405 were segregated according to animals (X^2 test, all $p < 0.05$), except for one animal (R887) for
406 which differences did not reach significance ($\chi^2 = 0.12$; $p = 0.73$; **Table 1**). As already noted,
407 for R887 there was under-sampling of gRSC cells (n=15 across 7 trials), possibly due to the
408 tract trajectory passing through white matter tracts before reaching gRSC. We concluded that
409 while the majority of gRSC non-directional cells were theta-modulated, the majority of non-
410 directional cells in dRSC fired uncoupled from theta (see pie chart in **Figure 6)**.

411 Theta-strength (spike-LFP coupling) and rhythmicity (autocorrelograms) were assessed by
412 computing IC and IR, respectively (**Table 1**). At the single cell level, the average IC was
413 significantly higher in gRSC compared to dRSC (IC: gRSC (292), 0.15 ± 0.01; dRSC (350),
414 0.06 ± 0.003; WRS test, z = -10.09, $p < 0.001$). This reflects the overall larger proportion of
415 theta-modulated neurons in gRSC (**Figure 6**), as well as the stronger theta modulation-depth
416 within each of these neurons. In this respect, the firing of cells that reached the theta-
417 modulation criterion in gRSC was considerably more phase-locked to theta compared to the
418 same cells recorded in dRSC, which only displayed weak spike-LFP coherence (IC: gRSC
419 (196), 0.2 ± 0.01; dRSC (125), 0.1 ± 0.01; WRS test, z = 7.17, $p < 0.0001$; **Figure 3**).
420 Significant IC differences were confirmed when the analysis was performed individually for

421 each animal and no difference was observed between animals (**Table 1;** See **Supplementary**

422 **Figure 1** for phase preference analysis of the theta-rhythmic neurons).

423

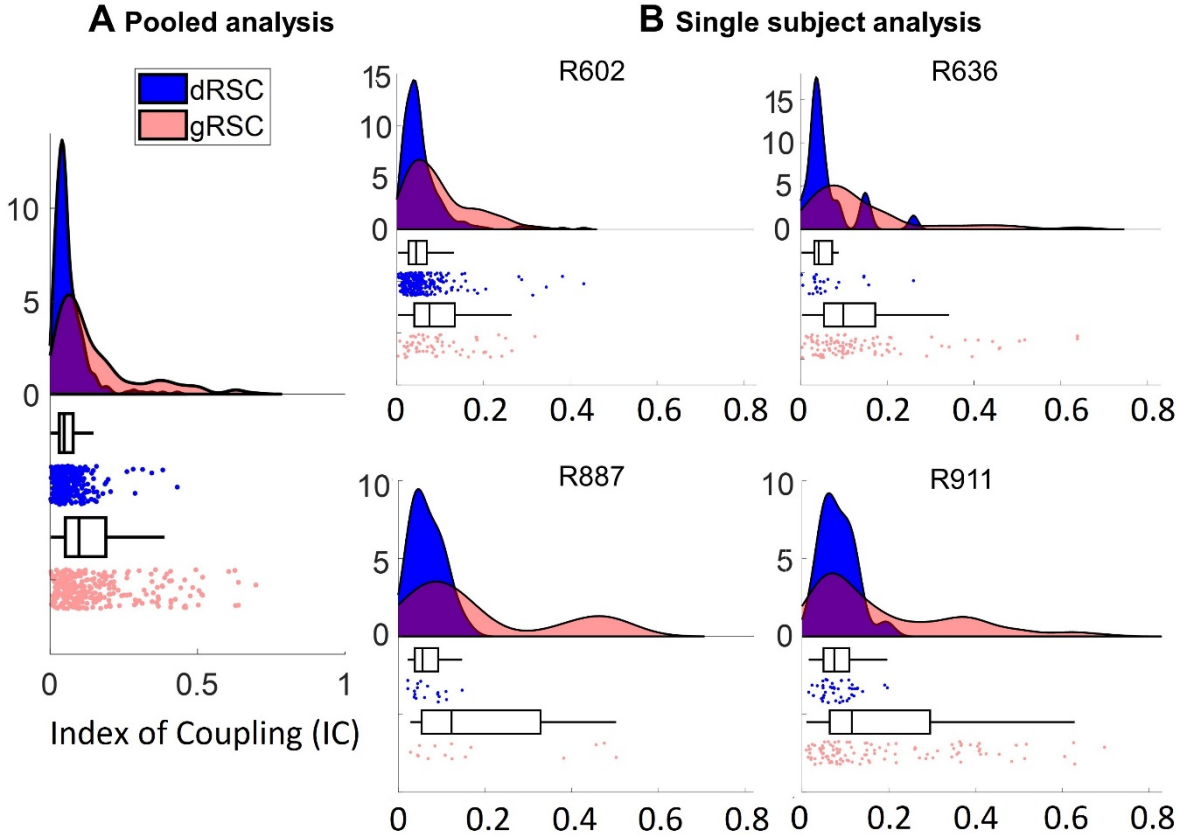

424

425 **Figure 3. Differences in theta-phase locking.** Distribution of ICs **(A)** for all cells and **(B)**

426 within each animal. (C) Distribution of IC considering only cells with firing significantly

427 coherent with theta (IC>99th percentile shuffling). Data is shown as a split violin plot + raw

428 jittered data point + boxplot. Split violin plots show the probability density function (PDF) of the

429 observed data points. Each marker is a cell (dRSC, blue; gRSC, red). gRSC: the higher average

430 IC reflects a larger proportion of neurons with firing locked to theta, as well as stronger theta-

431 modulation depth within each neuron.

Average IR was significantly higher and more positive in gRSC compared to dRSC when all cells were pooled into a single distribution (IR: gRSC, 0.04 ± 0.02; dRSC, -0.02 ± 0.01; WRS test, z = -4.61, $p < 0.0001$). In the single subject analysis, however, differences in IR did not reach a statistical significance in more than half of the experimental animals (3/4; only for R636; z = -2.09; $p = 0.04$; **Table 1**), albeit in all cases averages were higher in gRSC compared to dRSC. This is because some neurons (total, 49.53%; gRSC, 42.86%; dRSC, 60%) with significant phase-locking to theta did not show significant theta rhythmicity in their spike trains, suggesting spikes emitted at theta frequency for only brief periods of otherwise theta-unrelated spikes. This discrepancy, in which more cells fired phase-locked to theta than fired rhythmically, means that our classification criteria (based on IC) is sensitive to low amounts of locking, which can potentially occur in cells with non-rhythmical spiking, as previously reported for RSC (Eliav et al., 2018; Alexander et al., 2018) and ATN neurons (Albo et al., 2003). **Figure 4** displays examples of a theta phase-locked and rhythmic cell (high IC, IR>0.001), and a theta-locked but non-rhythmic cell (high IC, IR<=0.001). As can be seen, the main difference between the two cell types, aside from the autocorrelation differences (sinusoidal vs flat), is the degree of theta modulation and height of the baseline firing (firing at low-excitability phases) that is visible in the spike-phase histograms (iii). Theta phase-locked and rhythmic cells exhibit strong locking to the theta cycle and low baseline firing outside of a narrow oscillatory range, whereas phase locked and non-rhythmic cells exhibit weaker, and sometimes virtually no locking to theta and a higher baseline firing.

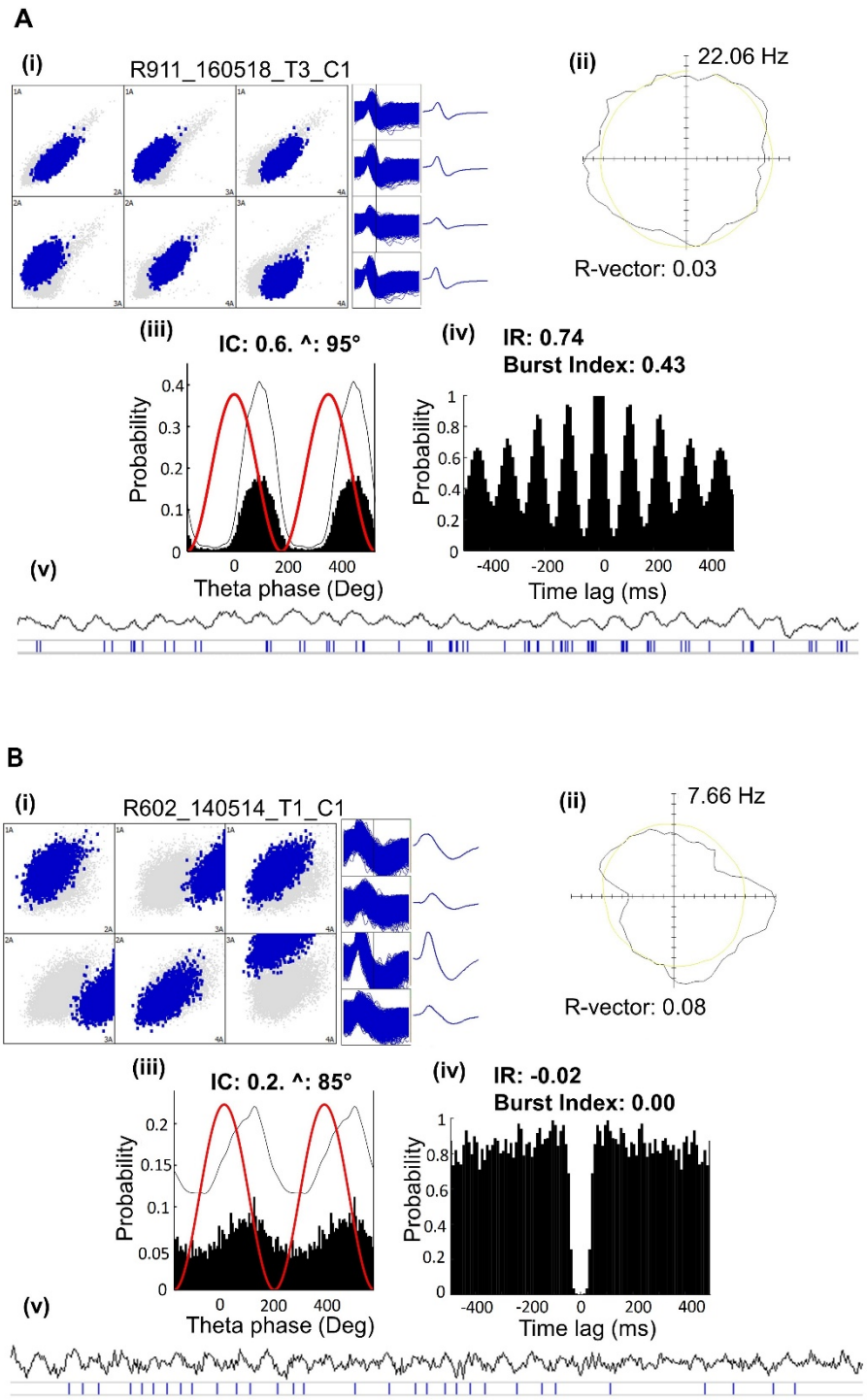

Figure 4. Two types of theta-modulated cells: (A) theta coupled and rhythmic vs (B) theta coupled and non-rhythmic. For each cell the following plots are shown, **(i)** Cluster space plots and associated tetrode spike waveforms. **(ii)** Polar plot of firing rate vs head direction, showing a

uniform directional firing distribution (Hz). Peak firing rate is reported next to each plot. Thinner line circle indicates dwell time distribution (seconds). **(iii)** Double-plotted histogram of spike frequency relative to theta phases. Thin line is the corresponding smoothed density estimates (see Methods). The thicker line is the sine wave representing two theta cycles. For cell (B), the spike-phase histogram displays weak locking and elevated baseline firing. **(iv)** Temporal autocorrelogram showing theta-frequency rhythmicity for (A) but non-rhythmical firing for (B). **(v)** Spike raster and corresponding unfiltered LFP signal recorded from the same tetrode. Each trace shows 3s of recordings. Cell (A) fires rhythmic spike trains, roughly corresponding to the frequency of LFP. In contrast, theta-modulation is not visually detectable in the LFP traces of (B), and here is based on IC > 99th percentile shuffling.

3.1.4 gRSC cells have higher firing rate and spike bursting propensity

In addition to differences in the intrinsic oscillation of single cells, gRSC and dRSC displayed a number of other interesting differences in their temporal firing properties. gRSC cells fired with significantly higher mean firing rates compared to dRSC (mean firing rate: gRSC, 4.63 ± 8.61Hz; dRSC, 3.13 ± 3.6Hz; WRS test, z = 2.73, $p < 0.01$). Furthermore, gRSC cells displayed a higher propensity to burst. In gRSC, 88/292 cells (30%) fired in bursts with peak ISI <10ms, compared to only 41/350 cells (11.7%) in dRSC ($\chi^2 = 33.65$; $p < 0.0001$). The prevalence of bursting units in gRSC was reflected in a significantly higher average burst index (burst index: gRSC, 0.08 ± 0.01; dRSC, 0.04 ± 0.01; WRS test, z = -6.30, $p < 0.001$). **Figure 5** shows examples of bursting and non-bursting units. Among bursting units, bursts were discharged rhythmically within theta frequencies in gRSC, but not dRSC where cells mostly burst at other frequencies (theta-bursting cells, gRSC, 76/88, 86.3%; dRSC, 17/41, 41.1%; $\chi^2 = 28.03$; $p < 0.0001$). Hence, theta-modulated cells were further subdivided into theta-modulated non-bursting cells (gRSC, n = 120 vs dRSC, n = 108), and theta-bursting

481 cells (gRSC, n = 76 vs dRSC, n = 17). Theta-modulated cells emitted compact spike trains at
482 theta frequency, without bursts, as their ISI reached values >10ms. In contrast, theta-bursting
483 cells fired rhythmically at theta frequency with ISI <10ms. Differences in firing frequency
484 and burst index were maintained when data were segregated according to animal, and again
485 no difference was found between animals (all $p < 0.05$; **Table 1).** Overall, these results
486 confirm gRSC as a locus of theta-bursting neurons (**Figure 6**).

487

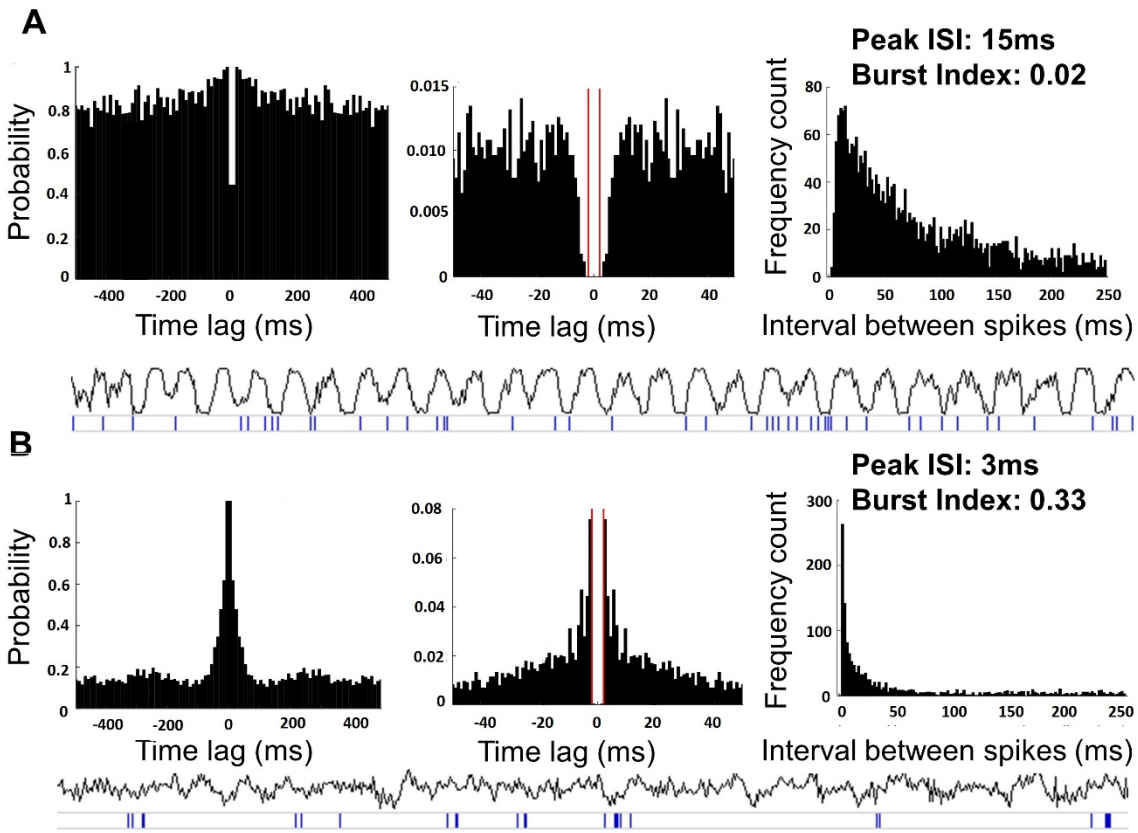

488

489 **Figure 5. Two types of temporal firing modes: (A)** non-bursting vs **(B)** bursting. Two
490 examples of non-theta-modulated cells. The following plots are shown. From left to right: (1)
491 Normalized temporal autocorrelogram implemented between ±500ms. (2) Temporal
492 autocorrelogram implemented between ±50ms: gaps at intervals < 2ms reflect the refractory

period; (3) Inter-spike interval (ISI) histogram and (4) plots of spiking events (bottom) relative to the raw LFP trace (top). Non-bursting unit (A): fires single spikes (in groups of 1-2) and displays a prevalence of long ISI. Bursting unit (B): spikes are emitted in groups of 2-3 spikes separated by ISI < 10ms, defined as a compact spike train. The prevalence of short ISI is reflected in a fast-decaying central peak of the ISI histogram and autocorrelogram, which can be contrasted to the less steep histogram peak in (A). Each spike train typically has a pause longer than 120ms before and after it, as firing is not aligned to theta.

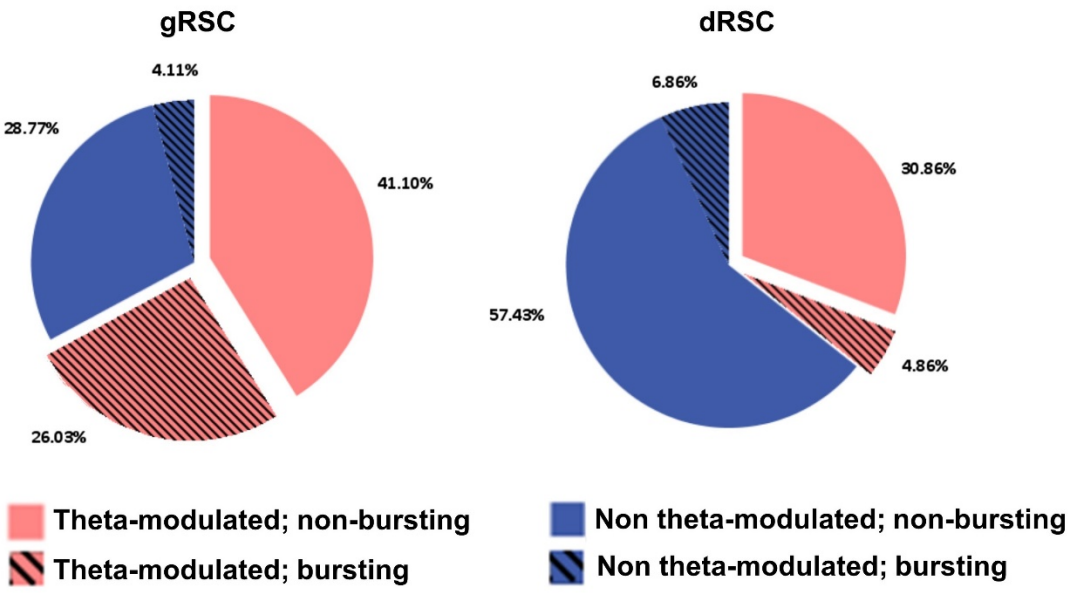

Figure 6. Theta-modulated cells are concentrated in the granular subregion of the RSC (gRSC). Theta-modulated and non-theta-modulated cells include bursting and non-bursting cells, divided based on peak ISI for the cell less than 10ms. gRSC: the majority of the cells fire coupled to the LFP theta, whereas most dysgranular RSC (dRSC) cells fire uncoupled from theta. gRSC also contains a higher proportion of bursting units, and the majority of these units are theta-bursting. In contrast, dRSC contains only a marginal subpopulation of bursting units, both theta and non-theta.

509 **3.1.5 Waveform differences: theta phase-locked cells have narrower waveforms**

510 Finally, we examined whether theta-modulated and non-theta modulated cells in RSC were
511 also morphologically distinct in their waveforms. We first examined the distribution of peak-
512 to-trough widths by fitting a two-Gaussian component, and two conservative cutoffs were
513 identified on this model to separate cells into narrow, broad and in-between (see Methods).
514 We discarded 28 cases because spike waveforms did not reach time for repolarization. The
515 analysis resulted in two modes (cell types): narrow spiking cells, 47.23%; broad spiking cells,
516 46.6%. A further 6.19% of cells were left unclassified based on values falling into the dip of
517 the bimodal distribution (**Figure 7**). The calibrated Hartigan's Dip Test discarded the null
518 hypothesis of unimodality (DIP = 0.062; $p < 0.001$). We then compared the firing
519 characteristics of cells in the two groups identified by the model. Cells classified as the
520 narrow spiking type displayed a higher proportion of theta-modulated cells (narrow, 196/290;
521 broad, 99/286; $\chi^2 = 62.65$, $p < 0.001$; **Figure 7**) and significantly stronger theta phase locking
522 (IC: narrow, 0.14 ± 0.009; broad, 0.06 ± 0.003; z = -6.80; $p < 0.001$) compared to the broad
523 type.

524 Cells were considered to be interneurons if the waveform peak-to-trough width was < 250µs
525 and mean firing rate was > 5Hz (Henze et al., 2000; McCormick et al., 1985). We compared
526 the proportion of interneurons between cell types and subregions. The proportion of
527 interneurons was significantly higher among theta-modulated cells compared to non-theta
528 modulated cells (theta-modulated: 63/321, 19.63%; non-rhythmic: 10/321, 3.12%; $\chi^2 = 43.42$,
529 $p < 0.001$). As a result, this proportion was significantly higher in gRSC compared to dRSC,
530 due to the anatomical organization of theta-modulated cells (gRSC: 39/292, 13.36%; dRSC:
531 12/350, 3.53%; $\chi^2 = 21.45$, $p < 0.001$). In agreement with the estimations based on

532 comparisons of proportions, a two-way ANOVA conducted on waveform peak-to-trough
533 widths found a main effect of cell type, $F(1,1) = 20.12$, $p < 0.001$, and brain region, $F(1,1) =$
534 18.38, $p < 0.001$, but no interaction, $F(1,1) = 3.57$, $p = 0.06$. According to these results, theta-
535 modulated cells, predominantly found in gRSC, displayed considerably shorter waveform
536 duration compared to non-theta modulated firing cells, predominantly found in dRSC (theta-
537 modulated: 295.26 ± 9.05µs; non-theta-modulated: 363.99 ± *7.36*µs; WRS test, z = -6.85, $p <$
538 0.0001). Average peak-to-trough width for gRSC cells were as follows: theta-modulated (n =
539 196), 266.02 ± 11.54µs; non-theta-modulated (n = 96), 343.54 ± 14.08µs. Average peak-to-
540 trough width for dRSC cells were as follows: theta-modulated (n = 125), 341.12 ± 13.66µs;
541 non-theta-modulated (n = 225), 372.71 ± 8.58µs. Between-subjects analysis confirmed a
542 narrower average waveform in gRSC compared to dRSC (gRSC, 291.51 ± 9.26µs; dRSC,
543 361.43 ± 7.39µs; WRS test, z = 6.68, $p < 0.001$). As seen in **Table 1**, this difference was
544 repeated in the within-subject analysis, albeit in one animal it was not significant (R636; z =
545 1.45; p =0.15). Collectively, these results suggest that a higher number of theta-modulated
546 cells are fast-spiking interneurons compared to cells that fire uncoupled from theta **(Figure 7)**.
547 Theta-modulated cells are therefore in a position to influence firing rates of neurons located
548 within the limits of the RSC, without transmitting rhythmic-modulation to the local head
549 direction cell population, to which they might be connected.

550

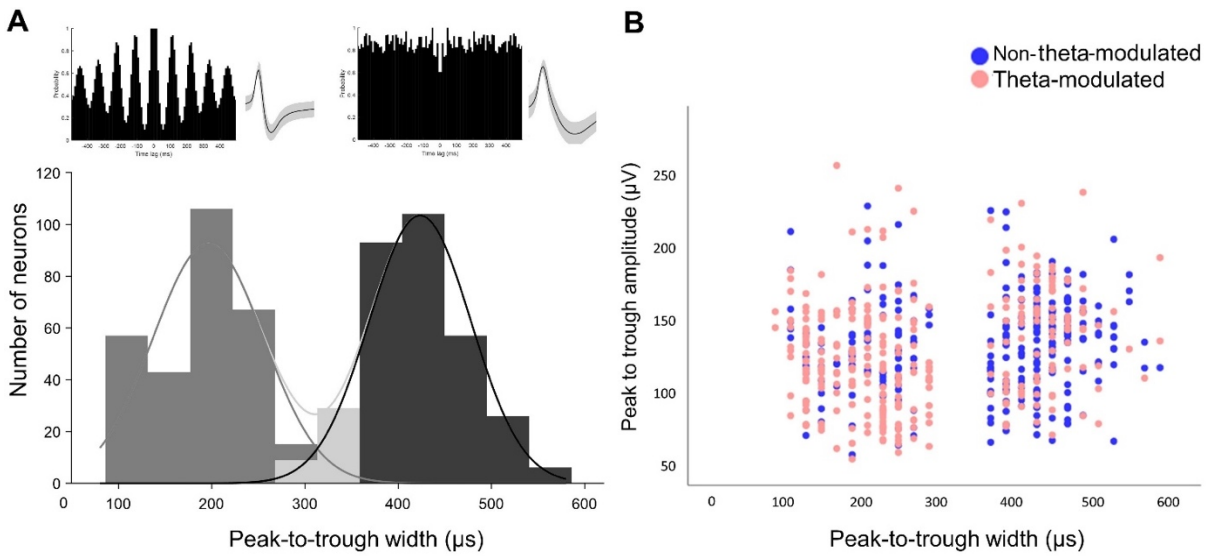

Figure 7. Broad and narrow spiking cells display differences in theta-modulation strength. **(A)** Distribution of the peak-to-trough width (µs) across all cells. Gaussian fits for the different modes (cell types) are displayed: broad (black), narrow (dark gray), and unclassified (light gray). Top, examples of autocorrelogram and averaged waveform for theta-modulated (left) and a non-theta-modulated (right) unit. Mean and standard deviation of the waveforms are shown. Theta-modulated cells tend to have spikes of shorter duration and a higher firing frequency than non-theta-modulated ones, suggestive of a higher prevalence of fast-spiking interneurons. **(B)** Waveform width of narrow and broad spiking cells in (A), plotted as a function of waveform amplitude (µV). A higher number of theta-modulated cells is found in the narrow group (n=196/290; 66.6%), whereas a higher number of non-theta-modulated cells is found in the broad group (n=187/286; 65.4%).

3.2 Retrograde tracer experiment

We next compared, using retrograde tracing, the thalamic afferents to gRSC and dRSC to see if they differ, supporting that these are distinct circuits. The findings have been divided

567 between those tracer injections approximately at the AP levels (-5.5 and -5.8 from bregma) of
568 the electrodes used in the electrophysiological studies and those injections placed more
569 rostrally or caudally within the RSC (see **Table 2**). Injections were performed in two different
570 laboratories (UCL, n = 6 animals; Cardiff University, n = 17 animals), thus providing an
571 internal replication for our findings (see **Supplementary Tables 3-4** for injection
572 coordinates).

573

574 **Table 2.** List of all retrograde tracer injections. 23 animals with a total of 29 injections.

Injections at electrode level (n=13)				
Case No.	***Injection site***	***Tracer***	***AV label***	***Laboratory***
222#9	dRSC s + d	CTB	AVVL	Aggleton; Cardiff
222#10	dRSC s + d	CTB	AVVL	Aggleton; Cardiff
077941#13	gRSC d	CTB	AVVL	Aggleton; Cardiff
077942#14	gRSC d	CTB	AVVL	Aggleton; Cardiff
878	dRSC, s + d	Ctb-488	AVVL	Jeffery; London
878	gRSC, s (d)	Ctb-594	AVVL/AVDM	Jeffery; London
731	dRSC, s + d	FG	AVVL	Jeffery; London
731	gRSC, s + d	Ctb-594	AVVL/AVDM	Jeffery; London
730	dRSC, d	Ctb-594	(AVVL)	Jeffery; London
730	gRSC s + d	FG	AVVL/AVDM	Jeffery; London
717	dRSC s + d; (M2)	FG	AVVL	Jeffery; London
729	dRSC s + d	FG	AVVL	Jeffery; London
682	gRSC s (d)	Ctb-594	AVVL/AVDM	Jeffery; London

Injections at rostral and caudal locations (n=16)				
Case No.	***Injection site***	***Tracer***	***AV label***	***Laboratory***
187#9	gRSC d (s) **(Rostral)**	BDA	AVVL	Aggleton; Cardiff
64#3	dRSC/M2/V2, s + d **(Rostral + caudal)**	FB	AVVL	Aggleton; Cardiff
172#27	dRSC (M2/V2), s + d **(Rostral + caudal)**	FB	AVVL	Aggleton; Cardiff
172#28	dRSC (M2/V2), s + d **(Rostral + caudal)**	FB	AVVL	Aggleton; Cardiff
225#4	dRSC s + d **(Rostral)**	CTB	AVVL	Aggleton; Cardiff
225#12	dRSC s + d/gRSC d **(Rostral)**	CTB	AVVL	Aggleton; Cardiff
223#1	dRSC s + d **(Rostral)**	CTB	AVVL	Aggleton; Cardiff
223#4	dRSC s+d/gRSC d **(Rostral)**	CTB	AVVL	Aggleton; Cardiff
227#22	dRSC s+d **(Rostral)**	FB	AVVL	Aggleton; Cardiff
227#22	dRSC d **(Caudal)**	CTB	AVVL	Aggleton; Cardiff
227#24	dRSC s + d **(Rostral)**	FB	AVVL	Aggleton; Cardiff
227#24	gRSC d **(Caudal)**	CTB	AVVL	Aggleton; Cardiff
227#16	dRSC d **(Rostral)**	CTB	AVVL	Aggleton; Cardiff
227#16	dRSC s+d/gRSC d **(Caudal)**	FB	AVVL	Aggleton; Cardiff
227#202	gRSC (dRSC) s + d **(Caudal)**	CTB	AVVL/AVDM	Aggleton; Cardiff
227#204	gRSC s + d **(Caudal)**	CTB	AVVL/AVDM	Aggleton; Cardiff
FB, fast blue; CTB, cholera toxin subunit b; BDA, biotinylated dextran amine; FG, fluorogold.				

575 The injection site indicates the center of the tracer deposit; s and d indicate superficial and deep layers of
576 the granular retrosplenial cortex (gRSC) or dysgranular RSC (dRSC). For deep injections, layer I was not
577 involved. Cases 187#9, 64#3, 172#27, 172#28 had multiple injections at both rostral and caudal locations.
578 Those regions and layers in parenthesis indicate weak involvement in the injection site. The third column
579 indicates the subfield of the anteroventral thalamic nucleus (AV) with densest cell label resulting from the
580 injection. AVDM, dorsomedial subfield of the AV; AVVL, ventrolateral subfield of the AV.

581 **3.2.1 Injections at the level of recording**

582 Thirteen retrograde tracer injections (n=10 animals) targeted RSC at approximately the same
583 AP levels as the recording sites (for representative injections see **Figure 9**; all injection sites
584 reported in **Table 2**). In three cases (730, 731 and 878), dual injections were made, one in
585 dRSC (n = 6) and the other in gRSC (n = 7; **Table 2**). For dRSC, all injections included
586 portions of both deep and superficial layers except a single injection (case R730) restricted to
587 the deep layers.

588 In all cases, retrogradely labelled cells were present in the ipsilateral thalamus, with varying
589 amounts of label in AD, AV, and the anteromedial nucleus (AM). Whereas both gRSC and
590 dRSC injections consistently resulted in widespread AD labelling, the distribution of labelled
591 cells within AV differed between the two injection sites. This difference within AV is the
592 focus of the results.

593 In all cases with injections largely confined to dRSC, retrograde cell label was virtually
594 restricted to the ventrolateral (AVVL) subfield of the AV nucleus (e.g., cases 222#10, 222#9).
595 In contrast, in four of the six cases that targeted gRSC (cases 878, 731, 730, 682), retrograde
596 cell label was observed in both AV subfields, i.e., AVVL and dorsomedial AV (AVDM). The
597 two remaining gRSC cases (077941#13, 077942#14) contained label in both AVVL and
598 AVDM, but the preponderance was in AVVL (**Figure 9**).

599 The overall pattern of differences (AVVL to dRSC; AVVL and AVDM to gRSC) can be
600 observed in **Figure 9,** which provides a schematic depicting the AV area with the densest cell
601 body labelling across the various injection cases (label in AD is not shown). In further support

602 of this difference in AV innervation, **Figure 10** shows photomicrographs of the two different
603 patterns of AV labelling in a single case (878) that had injections in both dRSC and gRSC.

604 We then correlated the variations in labelling with variations in injection site. For gRSC, in
605 the four cases with combined AVDM/AVVL label the injection site included both deep and
606 superficial layers (cases 878, 731, 730, 682), whereas in two cases where the label was
607 predominantly in AVVL, the gRSC injections were restricted to the deep layers (cases
608 077941#13, 077942#14; see **Figures 8 D, E; 9**).

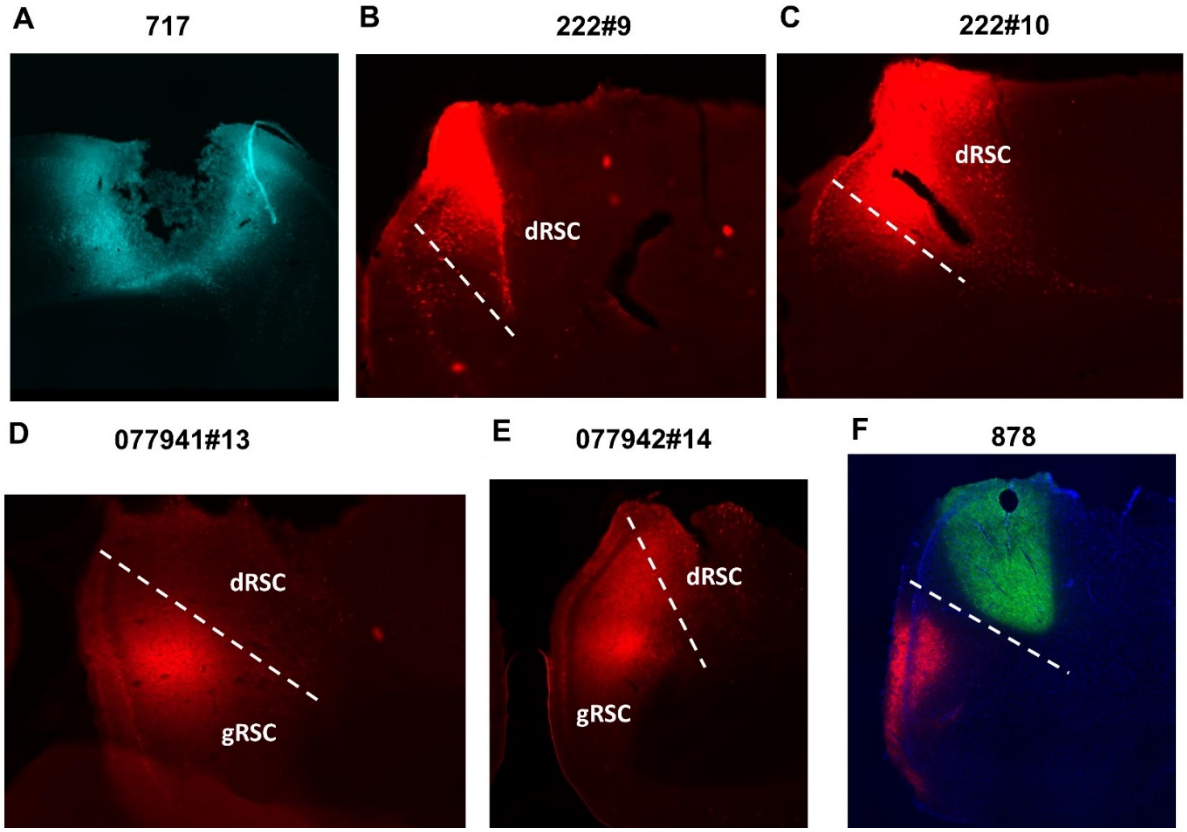

609

610 **Figure 8: Injections in retrosplenial cortex (RSC) were made at the electrode recording**
611 **levels.** Cholera toxin subunit b (CTB) and fluorogold (FG) injections in **(A-B-C)** dysgranular
612 RSC (dRSC, both superficial and deep layers) and **(D-E)** granular RSC (gRSC, mainly deep

layers). **(F)** Dual injection in granular (mainly superficial layers) and dysgranular (superficial and deep layers) RSC. AP level: -5.5mm.

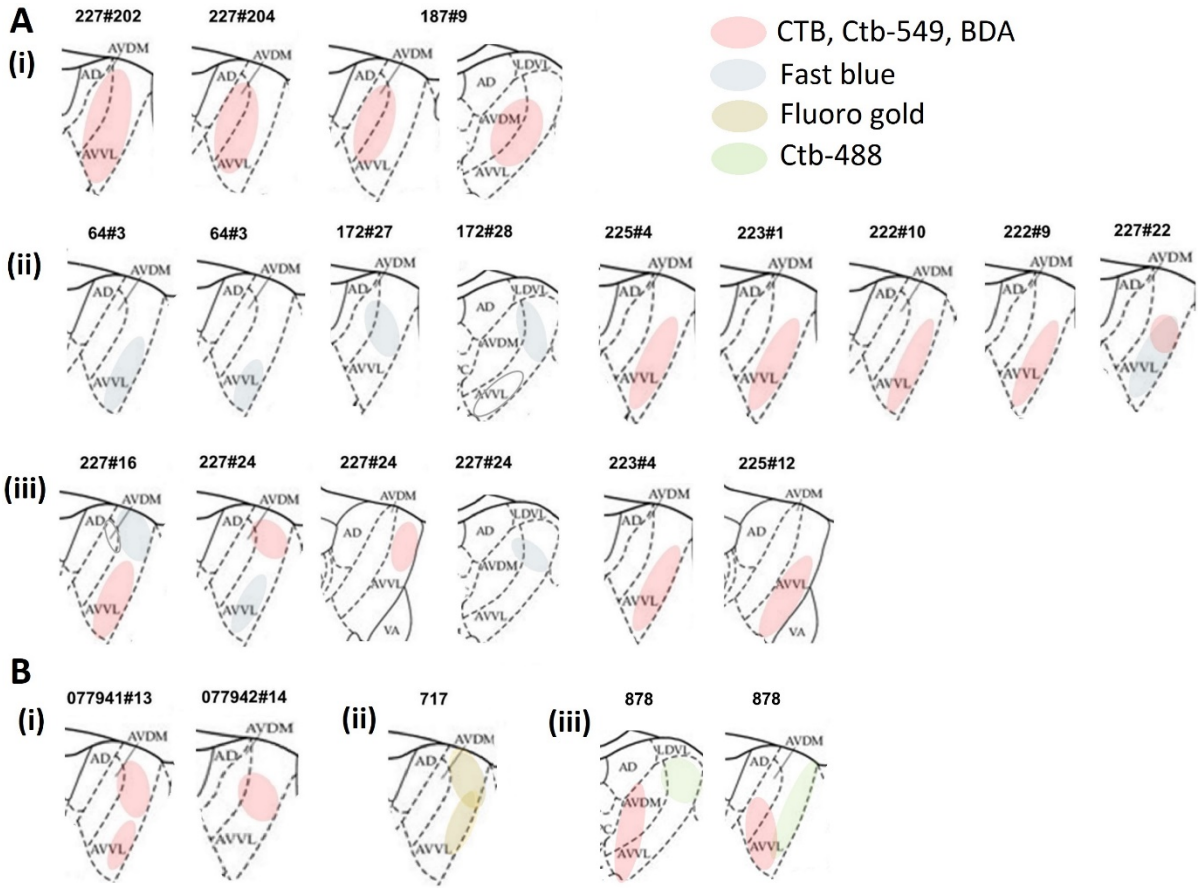

Figure 9. Ventrolateral AV (AVVL) widely projects to both gRSC and dRSC, dorsomedial AV (AVDM) projections are more restricted to superficial layers of gRSC. Schematics showing areas of retrograde cell labelling in AV**. (A)** Tracer injections rostral or caudal of electrode level; **(B)** injections at the electrode level. **(i)** AV label in cases of single tracer injection in gRSC. **(ii)** AV label in cases of single injection or multiple injections (127#27, 127#28, 54#3, 227#22) in dRSC. **(iii)** AV label in cases with combined gRSC and dRSC tracer injections. Cases 227#16, #24 and 878 have dual injections placed in dRSC and gRSC. Cases 223#4 and 225#12 have a combined injection in both gRSC and dRSC. Areas of label are color coded according to tracer type (see legend). For cases 227#16 and 172#28 there was weak additional labelling in AVDM and AVVL respectively, resulting from FB injection in dRSC

626 (empty circles). Abbreviations: AD, anterodorsal thalamic nucleus; AVVL and AVDM,
627 ventrolateral and dorsomedial subfields of the anteroventral thalamic nucleus; VA, ventral
628 anterior thalamic nucleus; LDVL, ventrolateral subfield of the laterodorsal thalamic nucleus.

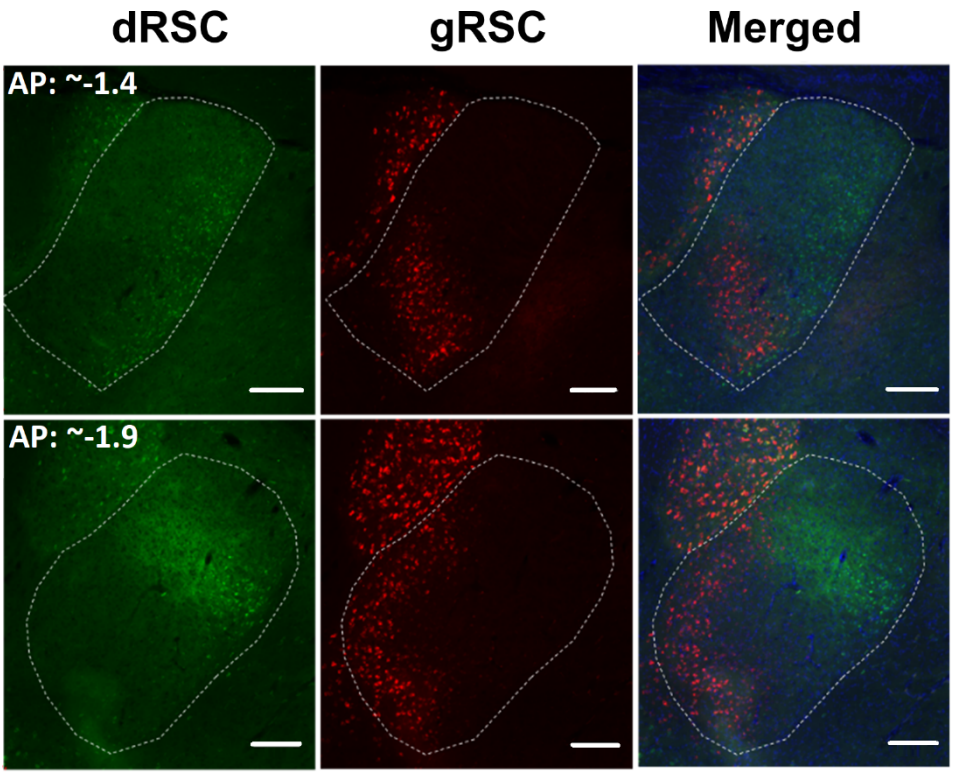

629

630 **Figure 10. Cell label is seen in AVDM following injections in superficial layers of gRSC,**
631 **and in AVVL following dRSC injections.** Dual retrograde tracer injections into dRSC (CTB-
632 488 green) and gRSC (CTB-549 red), with AV borders indicated. See injection sites in Figure 8
633 (Case 878). The photomicrographs show separate and combined images for two different AP
634 levels within the same animal. Cells labelled with CTB-488 (green; dRSC) are concentrated in
635 lateral AV, corresponding to AVVL, whereas CTB-549 label (red, gRSC) is also present more
636 medial, i.e., in both the AVVL and the AVDM subfields (see Figure 9 for schematic). Scale bars
637 200µm.

638 **3.2.2 Injections at more rostral and caudal RSC locations**

639 In a further sixteen retrograde tracer injections (n=13 animals), we targeted portions of RSC
640 >0.5 mm rostral or caudal to the electrophysiology recording sites (**Table 2;** for representative
641 injections see **Supplementary Figures 2-3**). Of these, six injections were from three cases
642 with dual tracer injections at different AP levels (**Supplementary Figure 2**). Nine tracer
643 injections seemed restricted to the dRSC, four to the gRSC and three included both RSC
644 subregions (**Supplementary Figure 3**). These dRSC injections included both superficial and
645 deep layers, except for two cases where the injections appeared restricted to deep dRSC
646 (rostral 227#16, caudal 227#22). Irrespective of AP level, we observed consistent labelling
647 differences after dRSC and gRSC injections (**Supplementary Figure 2**) that closely matched
648 those differences seen when the injections were placed at the level of the electrodes. Once
649 again, dRSC injections were consistently associated with AV label in AVVL (only
650 occasionally extending marginally into AVDM towards its dorsal border), while gRSC
651 injections resulted in label in both AVVL and AVDM **(Figure 9)**.

652 Further examples of these differential patterns of AV label can be see in **Figure 11.** This
653 figure contrasts when a tracer injection involved both dRSC and gRSC, versus when it was
654 located in just the dRSC subregion. An injection of CTB involving both RSC subregions
655 resulted in extensive cell labelling across both AVDM and AVVL (case 227#202; **Figure 11**
656 **A, B**). Meanwhile in a case with dual injections (case 227#16), the rostral dRSC injection
657 (CTB, red) resulted in ventral AVVL label, while the caudal fast blue injection (primarily
658 dRSC but also deep gRSC) labelled dorsal AVVL (case 227#16; **Figure 11 C, D**).

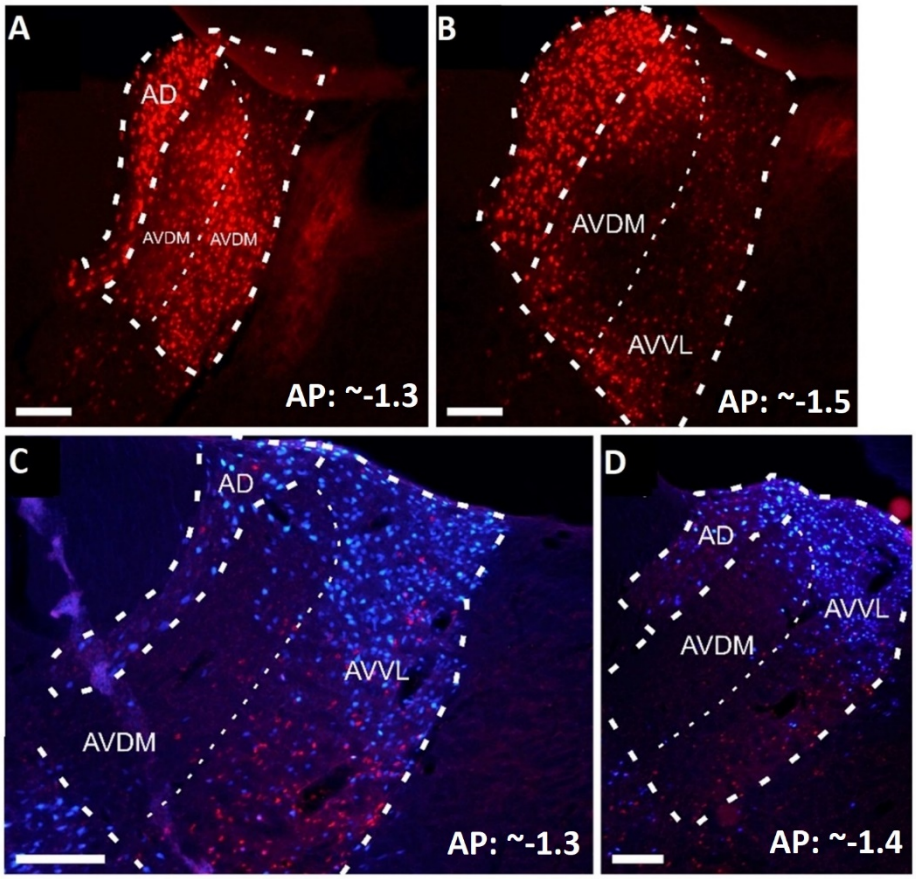

Figure 11. **Injections into both deep and superficial layers of gRSC (upper) result in more extensive and combined AVDM/AVVL label than is seen after dRSC injections (lower).** AVDM Photomicrographs depicting retrograde cell label after retrosplenial injections. **(A-B)** Cell label following a CTB injection in gRSC (case 227#202, superficial and deep layers). Retrograde labelled cells are seen in both AV subfields. See injection sites in Supplementary Figure 3. **(C-D)** Retrograde labelled cells following dual injections in dRSC at anterior (CTB) and posterior (FB) portions (case 227#16). See injection sites in Supplementary Figure 2. For both injections, cell labelling is predominantly present in the AVVL subfield, with more scattered cell label in the AVDM subfield (see Figure 8 for schematic). Two different APs are shown for the same animal. AD, anterodorsal thalamic nucleus; AVDM, dorsomedial subfield of AV; AVVL, ventrolateral subfield of AV. Scale bars 200µm.

672 In case 227#24 (**Figure 12**) separate injections were placed in rostral dRSC (fast blue,
673 involving deep and superficial layers) and in caudal gRSC (CTB, deep layers; see also
674 schematic **Figure 9**). This and other cases with dual injections positioned at rostral and caudal
675 portions of the RSC (cases 227#22 and 227#24, 227#16; **Figures 11-12**) also supported a
676 previously described topographical pattern (Shibata, 1993): namely, that ventral AV
677 preferentially projects to the rostral RSC whereas dorsal AV targets caudal RSC (see **Figure**
678 **11 C, D**). This same gRSC injection (227#24) showed a concentration of AVVL cell label
679 (**Figure 12**), whereas three other cases with gRSC injections resulted in combined
680 AVVL/AVDM cell label (cases 227#204, 227#202,187#9; as also described above for the
681 gRSC injections close to the AP of the recording sites see **Figures 8-9**).

682 Further inspection of these cases revealed that the single case with restricted AVVL label
683 (227#24) had a gRSC injection largely confined to its deep layers, whereas the three cases
684 with further AVDM involvement had either obvious (case 227#204; 227#202) or likely (case
685 187#9 – see **Supplementary Figure 3**) involvement of superficial layers in the injection sites.
686 These observations support the earlier conclusion that it is particularly the superficial layers of
687 gRSC that receive AVDM projections. In further agreement, the three remaining cases with
688 combined gRSC/dRSC injections had cell label in AVVL (but not AVDM) and in these cases
689 the gRSC portion of the injection sites seemed largely contained within the deep layers (cases
690 225#12, 225#4, 227#16).

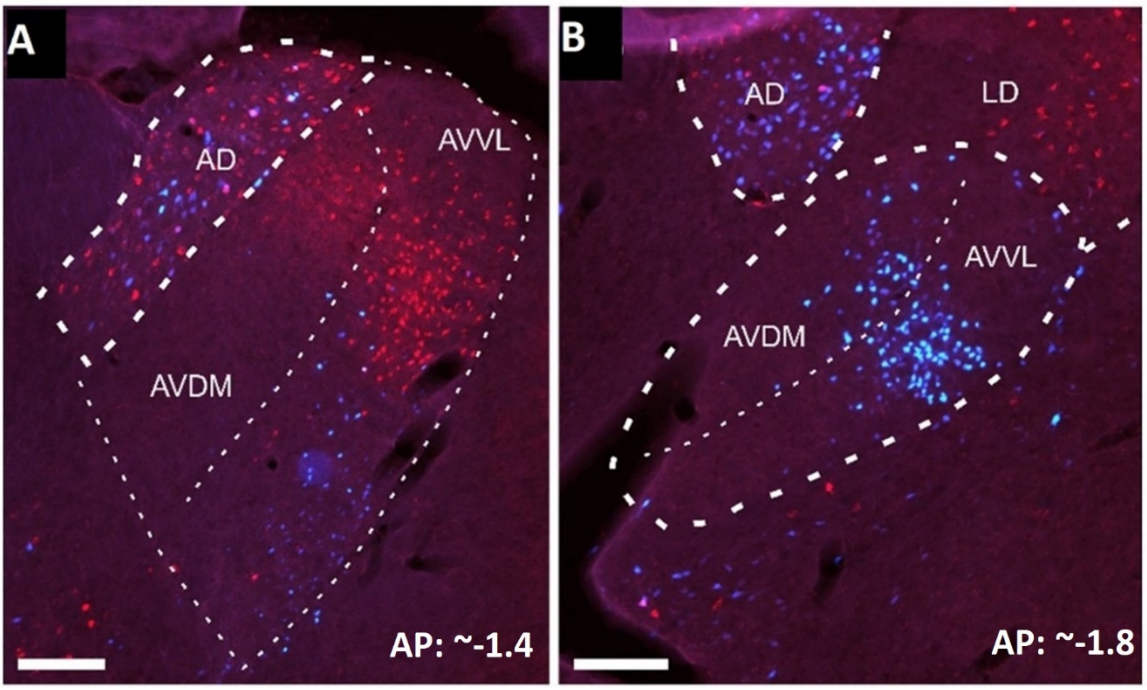

Figure 12. Injections positioned in deep layers of gRSC only and more moderately label a cell cluster in the AVVL, similarly to dRSC injections. Photomicrographs of AV label for case 227#2, after dual injections in gRSC (deep) and dRSC (superficial and deep), at two different AP levels. See injection sites in Supplementary Figure 2. Fast blue (blue) label originated from an injection centred in rostral dRSC (both superficial and deep layers) whereas cholera toxin-b label (red) originated from an injection centered in caudal gRSC (deep layers only). The majority of fast blue cell label is in AVVL subfield (see Figure 9 for schematic). Unusually for a gRSC injection, the retrograde label (red) was also largely confined to AVVL, potentially reflecting the deep location of the tracer injection. Two different APs are shown for the same animal. Abbreviations: AD, anterodorsal thalamic nucleus; AVDM, dorsomedial subfield of AV; AVVL, ventrolateral subfield of AV; LD, laterodorsal thalamic nucleus. Scale bars 200µm.

704 # 4.0 Discussion

705 As part of an ongoing attempt to understand the contribution of retrosplenial cortex to spatial
706 memory processing, we investigated what distinguishes its two principal subregions, granular
707 (gRSC) and dysgranular (dRSC). Recent findings of landmark-sensitive directional neurons
708 restricted to the dysgranular region only (Jacob et al., 2017) have suggested that RSC may
709 comprise two subcircuits, one (gRSC) more connected to hippocampus and the other (dRSC)
710 more connected to sensory regions. We thus investigated whether there are
711 electrophysiological or anatomical differences that shed light on this dichotomy.
712 Electrophysiologically, we compared the temporal firing characteristics, waveform
713 characteristics and relation to the local LFP of non-directional cells recorded from gRSC and
714 dRSC during free exploration in rats, finding greater coupling with theta oscillations in gRSC
715 compared to dRSC. Anatomically, we used retrograde tracing to label gRSC and dRSC
716 projections from one of the main inputs to RSC, the anterior thalamus, to see if there might be
717 differential projections from this region; we found that gRSC was distinguished by a
718 projection from the dorsomedial subfield of the anteroventral thalamus (AVDM) that was
719 much weaker or missing following the dRSC injections. Below, we examine these findings,
720 and then conclude with some speculations about the possible functional role of these two
721 thalamocortical subcircuits.

722 ## 4.1 Increased theta coupling in gRSC

723 Comparison of the two subregions (in both pooled and single subject analysis) revealed that
724 gRSC had a much higher mean IC (index of theta phase-coupling), firing frequency and
725 spike-bursting propensity, and theta-modulated cells in this region exhibited considerably

726 larger theta-modulation depth. However, we found no difference in local field potential (LFP)
727 theta oscillations between the two subregions, highlighting a dissociation between theta
728 rhythms in the LFP and oscillations present at the single cell level (i.e., theta rhythms are not
729 generated uniquely from local ensemble activity within gRSC, in line with results of Young and
730 McNaughton, 2009; Borst et al., 1987, Talk et al., 2004). These observations raise two
731 questions: what causes these differences and what, if any, are their functional implications?

732 One possibility is that these signals are a consequence of differential network connectivity
733 between gRSC/dRSC and the medial septal theta "clock." Septal GABAergic neurons express
734 theta-modulated firing and innervate both CA1 and gRSC – but dRSC much less so – with a
735 common projection pattern (Unal et al., 2015). They selectively target and inhibit GABAergic
736 interneurons, resulting in a rhythmic disinhibition of the principal neurons, the activity of
737 which thus becomes phase-locked to septo-hippocampal theta. Rhythmic disinhibition
738 supplied by the medial septum has been demonstrated to drive hippocampal theta activity
739 (Hangya et al., 2009) and could offer a similar explanation for the concentration of theta cells
740 in gRSC. Given the lack of septal input to dRSC, some dRSC neurons might become locked
741 to theta indirectly via cell-to-cell projections from gRSC theta cells.

742 An alternative possibility is that theta is modulated by the strong anterior thalamic projection
743 to RSC (both gRSC and, more moderately to, dRSC). Like cells in the medial septum, theta
744 rhythmically discharging cells in the AV fire locked to the local and hippocampal theta
745 oscillations, and these oscillations are strongly coherent (Albo et al., 2003; Vertes et al., 2001;
746 Tsanov et al., 2011, 2010). The medial mammillary bodies distribute massively to the AV via
747 the mammillothalamic tract (Seki and Zyo, 1984; Shibata 1992), and projects to the AV a
748 theta signal that combines tegmental, septal, and hippocampal theta activity (see reviews by

749 Vertes et al., 2004; Vertes and Kocsis, 1997). A role of the mammillary bodies-AV axis in
750 complementing the septo-hippocampal theta system (Zakowski et al., 2017; Ruan et al., 2017)
751 may explain the occasional report of theta oscillations in gRSC that persist or are enhanced in
752 the absence of hippocampal theta (i.e., during hippocampal large amplitude irregular activity,
753 Young and McNaughton, 2009; or electrolytic septal lesions, Borst et al., 1987). A third
754 possibility is that gRSC inherits theta rhythmicity via its stronger afferent connections with
755 the dorsal hippocampus, both from CA1 (Haugland et al., 2019; van Groen and Wyss, 1990;
756 Opalka et al., 2020; Unal et al., 2015) and subiculum, which is the major output of the
757 hippocampus and sends a strong projection to gRSC, but not dRSC (Meibach and Siegel,
758 1977). We emphasize that these options are not mutually exclusive. Thus, the AV may exert
759 an excitatory rhythmical influence on target cortical neurons receiving converging
760 hippocampal or septal projections (Yamawaki et al., 2019), which may be crucial for allowing
761 a subcortically-mediated regulation of coordinated hippocampus-RSC communication
762 (Chambers et al., 2021).

763 The second major question arising from the differential theta coupling observed between
764 gRSC and dRSC is what, if any, might be the functional consequences. Theta is widely
765 thought to have the function of synchronizing the excitability of brain regions throughout the
766 hippocampal formation (Korotkova et al., 2018), perhaps to facilitate information transfer or
767 synaptic plasticity. Within hippocampus itself, each theta cycle contains a sequential
768 activation of hippocampal neurons (usually manifesting as place cells) and may function to
769 organize sequential information as part of a spatio-temporal memory system. It may be that
770 gRSC with its greater hippocampal connectivity has the role of mediating between incoming

771 sensory information and ongoing spatial computations, with theta facilitating the transfer and
772 maintaining the spatio-temporal organization. We will return to this point later.

773 **4.2 Differential AV projections to gRSC and dRSC**

774 Our dataset of retrograde tracer injections adds to previous anatomical descriptions of anterior
775 thalamic inputs to RSC. Overall, in agreement with previous studies (Shibata, 1993), a
776 topography emerged from our tracing studies such that ventral AV projects to rostral RSC
777 while dorsal AV projects to caudal RSC. Within the AV projections, we found a clear
778 differentiation of AVDM and AVVL projections into the gRSC and dRSC. The AVVL
779 subfield targeted both retrosplenial subregions, providing moderate fiber input to both
780 superficial and deep layers (see also Van Groen and Wyss, 1990a, 1992, 2003; Shibata, 1993).
781 In contrast, the AVDM subfield provided a selective projection to the gRSC; mainly to the
782 superficial layers (Shibata, 1993). Overall, the present results argue for the presence of two
783 related but distinct AV-RSC subcircuits: AVVL to dRSC, AVVL and AVDM to gRSC.

784 Two anatomical facts are relevant for clarifying the observed variations in the
785 electrophysiology data between gRSC and dRSC. First, the difference in the overall
786 projection strength to the two RSC subregions should be noted, in addition to the
787 topographical organization of AV projections from within AV to each of these subregions
788 (Shibata et al., 1993). In relation to the first point, our data demonstrate stronger AV
789 projections to gRSC compared to dRSC (see also Van Groen and Wyss, 2003). Second, there
790 are differences in the source of these projections from different AV subfields. Superficial
791 gRSC layers receive a distinct projection from AVDM, which sends no or only moderate
792 projections to dRSC. In contrast, dRSC only receives widespread AVVL projections. Hence,

observed differences in theta modulation across the RSC might not simply be an effect of variations in AV fiber density (stronger AV to gRSC) but may also be explained by considering anatomically distinct cell populations within the AV projecting to the two RSC subregions.

4.3 Two interacting thalamocortical subcircuits

Previous behavioral, connectivity and neuroanatomical evidence, together with our current findings, combine to indicate that the RSC is not a unitary structure (see Aggleton et al., this issue, for review). gRSC is more strongly coupled with the hippocampal formation, as evidenced by both anatomical connectivity and theta modulation: the latter of which accords with the fact that theta is a distinguishing feature of neurons in brain regions that are linked to the hippocampal spatial system (Burgess et al., 2002; Buzsáki, 2002, 2005, Hasselmo and Eichenbaum, 2005; Buzsáki and Moser, 2013). Our findings add to this picture by showing that there is a selective contribution of the AVDM to this network, via gRSC. Future work will need to determine the distinct physiological properties of AVDM neurons, and the consequence on gRSC processing of removing this projection.

By contrast, dRSC is dominated by visual interactions (Fischer et al., 2020; Powell et al., 2020; Keshavarzi et al., 2021, van Groen and Wyss, 1992, 1990b,c; Van Groen and Wyss, 2003; Cooper and Mizumori, 2001; Pothuizen et al., 2009). This conclusion is bolstered by the recent findings of Jacob et al. (2017), who demonstrated stronger visual responsiveness in dRSC directional signals, which suggested a partial uncoupling from the main, hippocampally interacting head direction signal. The question thus arises: why does the brain maintain these separable subsystems?

815 One possibility is that this separation allows for the comparison of two information streams
816 that may agree or differ in their content, and thus allow for comparison and appropriate error
817 correction. The streams in RSC comprise interoceptive signals arising from subcortical
818 regions and exteroceptive signals coming in from the sensory periphery. A specific example
819 of these converging information streams is provided by the RSC head direction signal, which
820 arises from convergence of self-motion inputs (primarily interoceptive cues such as vestibular
821 signals, motor efference and proprioception) and static environmental information from the
822 sensory cortices (Yoder and Taube, 2014). The findings of Jacob et al (2017) that
823 directionally tuned neurons in dRSC operate independently of this "consensus" head direction
824 signal have suggested that RSC may be the site of weighted cue integration between the
825 current estimate of head direction and incoming sensory information (Page and Jeffery, 2018).
826 A similar principle may account for RSC processing more generally: that is, the gRSC input
827 from thalamus may supply an estimate of a current state, the dRSC supplies current sensory
828 input, and intrinsic connections between the subregions could allow for integration and
829 weighted cue combination. Thus, via intrinsic granular-dysgranular interconnections (Shibata
830 et al., 2009; Sugar et al., 2011), RSC can mediate exchange and integration of information
831 between more cognitive and more perceptual computations.

832 **4.4 Conclusion and future directions**

833 Our results detail differences in theta-related spiking between gRSC and dRSC along with the
834 existence of two interdependent AV-RSC subnetworks, suggesting two distinct streams of
835 information to the RSC. We propose that these conform to a more interoceptive stream that
836 conveys the results of internal processing and a more exteroceptive stream that conveys the

state of the external world as assessed by the senses. The cognitive stream is characterized by close connectivity with the hippocampal system, as well as a unique input from the AVDM. This convergence may represent a key aspect of RSC function, consistent with evidence from human neuroimaging studies showing a role for RSC in monitoring landmark stability (Auger et al., 2012) and integrating across scenes and reference frames (Sherrill et al., 2013; Marchette et al., 2014; Bicanski and Burgess, 2016; Byrne et al., 2007). In the future, a complete understanding of the limbic system will necessarily need to consider the inter-related functions of these subnetworks, rather than the function of either AV or RSC as a whole.

Acknowledgments

The authors would like to thank Roddy M. Grieves and James Street for the continued advice throughout these experiments and help with programming. We thank Pierre-Yves Jacob for his contribution to the collection of electrophysiology. The authors are grateful to Brook Perry for advice on the LFP analysis.

This work was supported by three Advanced Investigator Grants: KJ was supported by grants from Wellcome (103896AIA) and the Royal Society (IEC\R2\181140). ASM was supported by a Wellcome Trust Senior Research Fellowship (WT 110157/Z/15/Z). JPA and MM were supported by grants from Wellcome (103722/Z14/Z) and the UK BBSRC (BB/T007249/1).

EL was supported by a Medical Sciences Graduate School Studentship, University of Oxford: Clarendon Fund – Department of Experimental Psychology –Somerville College Mary Somerville Graduate Studentship (SFF1718_CB2_ MSD_1074636). N.Z. was supported by a scholarship from the China Scholarship Council (201608000007).

Data sharing

Data supporting the findings of this study are available on request from the corresponding author, Eleonora Lomi. Email address: eleonora.lomi@some.ox.ac.uk

Authors contributions

All authors discussed and reviewed the results. E.L. wrote the manuscript with input from all authors, who reviewed and edited the manuscript. In addition:

EL: Conceptualization and investigation of the project; Analysis of electrophysiology data; Data interpretation; Visualization.

MM: Collection and analysis of neurotracing data; Data interpretation.

HYC: Collection and analysis of neurotracing data.

NZ: Collections of electrophysiology data.

JPA: Funding acquisition; Resources; Supervision.

ASM: Conceptualization and administration of the project; Funding acquisition; Resources; Supervision.

KJ: Conceptualization and administration of the project; Protocol design; Funding acquisition; Resources; Supervision.

Competing interests

The authors declare the following competing interests: K.J. is a non-shareholding director of Axona Ltd.

References

Aggleton, J., Neave, N., Nagle, S., and Sahgal, A. (1995). A comparison of the effects of medial prefrontal, cingulate cortex, and cingulum bundle lesions on tests of spatial memory: evidence of a double dissociation between frontal and cingulum bundle contributions. *J Neurosci*, 15(11):7270–7281.

Aggleton, J. P., O'Mara, S. M., Vann, S. D., Wright, N. F., Tsanov, M., and Erichsen, J. T. (2010). Hippocampal–anterior thalamic pathways for memory: uncovering a network of direct and indirect actions. *Eur J Neurosci*, 31(12):2292–2307.

Aggleton, J. P. and Pearce, J. M. (2001). Neural systems underlying episodic memory: insights from animal research. *Phil Trans Royal Society London. Series B*, 356(1413):1467–1482.

Aggleton, J. P., Vann, S. D., Oswald, C. J., and Good, M. (2000). Identifying cortical inputs to the rat hippocampus that subserve allocentric spatial processes: a simple problem with a complex answer. *Hippocampus*, 10(4):466–474.

Albo, Z., Viana Di Prisco, G., and Vertes, R. P. (2003). Anterior thalamic unit discharge profiles and coherence with hippocampal theta rhythm. *Thalamus & Related Systems*, 2(2):133–144.

Alexander, A. S., Carstensen, L. C., Hinman, J. R., Raudies, F., Chapman, G. W., and Hasselmo, M. E. (2020). Egocentric boundary vector tuning of the retrosplenial cortex. *Sci Advances*, 6(8):eaaz2322.

Alexander, A. S., Rangel, L. M., Tingley, D., and Nitz, D. A. (2018). Neurophysiological signatures of temporal coordination between retrosplenial cortex and the hippocampal

formation. *Behav Neurosci*, 132(5):453–468.

Ardid, S., Vinck, M., Kaping, D., Marquez, S., Everling, S., and Womelsdorf, T. (2015). Mapping of Functionally Characterized Cell Classes onto Canonical Circuit Operations in Primate Prefrontal Cortex. *J Neurosci*, 35(7):2975–2991.

Auger, S. D., Mullally, S. L., and Maguire, E. A. (2012). Retrosplenial Cortex Codes for Permanent Landmarks. *PLOS ONE*, 7(8):e43620.

Berens, P. (2009). CircStat: A MATLAB Toolbox for Circular Statistics. *J Statistical Software*, 31(1):1–21. Number: 1.

Bicanski, A. and Burgess, N. (2016). Environmental Anchoring of Head Direction in a Computational Model of Retrosplenial Cortex. *J Neurosci*, 36(46):11601–11618.

Borst, J. G., Leung, L. W., and MacFabe, D. F. (1987). Electrical activity of the cingulate cortex. II. Cholinergic modulation. *Brain Res*, 407(1):81–93.

Braak, H. and Braak, E. (1991). Neuropathological stageing of Alzheimer-related changes. *Acta Neuropathologica*, 82(4):239–259.

Burgess, N., Maguire, E. A., and O'Keefe, J. (2002). The human hippocampus and spatial and episodic memory. *Neuron*, 35(4):625–641.

Buzsáki, G. (2002). Theta Oscillations in the Hippocampus. *Neuron*, 33(3):325–340.

Buzsáki, G. (2005). Theta rhythm of navigation: link between path integration and landmark navigation, episodic and semantic memory. *Hippocampus*, 15(7):827–840.

Buzsáki, G. and Moser, E. I. (2013). Memory, navigation and theta rhythm in the hippocampal-entorhinal system. *Nat Neurosci*, 16(2):130–138.

Byrne, P., Becker, S., and Burgess, N. (2007). Remembering the past and imagining the future. *Psychological Rev*, 114(2):340–375.

Caplan, J. B., Madsen, J. R., Schulze-Bonhage, A., Aschenbrenner-Scheibe, R., Newman, E. L., and Kahana, M. J. (2003). Human Oscillations Related to Sensorimotor Integration and Spatial Learning. *J Neurosci*, 23(11):4726–4736.

Cenquizca, L. and Swanson, L. (2007). Spatial Organization of Direct Hippocampal Field CA1 Axonal Projections To the Rest of the Cerebral Cortex. *Brain Res Rev*, 56:1–26.

Chambers, A. R., Berge, C. N., and Vervaeke, K. (2021). Cell-type-specific silence in thalamocortical circuits precedes hippocampal sharp-wave ripples. *bioRxiv*, 2021.05.05.442741.

Chen, L. L., Lin, L.-H., Barnes, C. A., and McNaughton, B. L. (1994). Head-direction cells in the rat posterior cortex. *Exp Brain Res*, 101(1):24–34.

Cho, J. and Sharp, P. (2001). Head direction, place, and movement correlates for cells in the rat retrosplenial cortex. *Behav Neurosci*, 115:3–25

Clark, B. J. and Taube, J. S. (2012). Vestibular and attractor network basis of the head direction cell signal in subcortical circuits. *Front Neural Circuits*, 6.

Climer, J. R., DiTullio, R., Newman, E. L., Hasselmo, M. E., and Eden, U. T. (2015). Examination of rhythmicity of extracellularly recorded neurons in the entorhinal cortex. *Hippocampus*, 25(4):460–473.

Cooper, B. G. and Mizumori, S. J. (1999). Retrosplenial cortex inactivation selectively impairs navigation in darkness. *NeuroReport*, 10(3):625–630.

Cooper, B. G. and Mizumori, S. J. (2001). Temporary inactivation of the retrosplenial cortex causes a transient reorganization of spatial coding in the hippocampus. *J Neurosci*, 21(11):3986–4001.

Dillingham, C. M., Milczarek, M. M., Perry, J. C., Frost, B. E., Parker, G. D., Assaf, Y., Sengpiel, F., O'Mara, S. M., and Vann, S. D. (2019). Mammillothalamic disconnection alters hippocampo-cortical oscillatory activity and microstructure: Implications for diencephalic amnesia. *J Neurosci*, 39 (34) 6696-6713.

Eliav, T., Geva-Sagiv, M., Yartsev, M. M., Finkelstein, A., Rubin, A., Las, L., and Ulanovsky, N. (2018). Nonoscillatory Phase Coding and Synchronization in the Bat Hippocampal Formation. *Cell*, 175(4):1119–1130.e15.

Fanselow, E. E., Sameshima, K., Baccala, L. A., and Nicolelis, M. A. L. (2001). Thalamic bursting in rats during different awake behavioral states. *PNAS*, 98(26):15330–15335.

Fischer, L. F., Mojica Soto-Albors, R., Buck, F., and Harnett, M. T. (2020). Representation of visual landmarks in retrosplenial cortex. *eLife*, 9:e51458.

Frank, L. M., Brown, E. N., and Wilson, M. A. (2001). A Comparison of the Firing Properties of Putative Excitatory and Inhibitory Neurons From CA1 and the Entorhinal Cortex. *J Neurophys*, 86(4):2029–2040.

Gabriel, M., Sparenborg, S. P., and Stolar, N. (1987). Hippocampal control of cingulate cortical and anterior thalamic information processing during learning in rabbits. *Experimental Brain Res*, 67(1):131–152.

Hangya, B., Borhegyi, Z., Szilágyi, N., Freund, T. F., and Varga, V. (2009). GABAergic neurons of the medial septum lead the hippocampal network during theta activity. *J Neurosci*, 29(25):8094–8102.

Hasselmo, M. E. and Eichenbaum, H. (2005). Hippocampal mechanisms for the context-dependent retrieval of episodes. *Neural Networks*, 18(9):1172–1190.

Haugland, K. G., Sugar, J., and Witter, M. P. (2019). Development and topographical organization of projections from the hippocampus and parahippocampus to the retrosplenial cortex. *Eur J Neurosci*, 50(1):1799–1819.

Henze, D. A., Borhegyi, Z., Csicsvari, J., Mamiya, A., Harris, K. D., and Buzsáki, G. (2000). Intracellular features predicted by extracellular recordings in the hippocampus in vivo. *J Neurophysi*, 84(1):390–400.

Hyman, J. M., Wyble, B. P., Goyal, V., Rossi, C. A., and Hasselmo, M. E. (2003). Stimulation in hippocampal region CA1 in behaving rats yields long-term potentiation when delivered to the peak of theta and long-term depression when delivered to the trough. *J Neurosci,* 23(37):11725–11731.

Jacob, P.-Y., Casali, G., Spieser, L., Page, H., Overington, D., and Jeffery, K. (2017). An independent, landmark-dominated head direction signal in dysgranular retrosplenial cortex. *Nat Neurosci*, 20(2):173–175.

Jinno, S., Klausberger, T., Marton, L. F., Dalezios, Y., Roberts, J. D. B., Fuentealba, P., Bushong, E. A., Henze, D., Buzsáki, G., and Somogyi, P. (2007). Neuronal Diversity in GABAergic Long-Range Projections from the Hippocampus. *J Neurosci*, 27(33):8790–8804.

Kadir, S. N., Goodman, D. F. M., and Harris, K. D. (2014). High-dimensional cluster analysis with the Masked EM Algorithm. *Neural Computation*, 26(11):2379–2394.

Keshavarzi, S., Bracey, E. F., Faville, R. A., Campagner, D., Tyson, A. L., Lenzi, S. C., Branco, T., and Margrie, T. W. (2021). The retrosplenial cortex combines internal and external cues to encode head velocity during navigation. *bioRxiv*, 2021.01.22.427789.

Korotkova, T., Ponomarenko, A., Monaghan, C. K., Poulter, S. L., Cacucci, F., Wills, T., Hasselmo, M. E., and Lever, C. (2018). Reconciling the different faces of hippocampal theta: The role of theta oscillations in cognitive, emotional and innate behaviors. *Neurosci Biobehav Rev*, 85:65–80.

Lewicki, M. S. (1998). A review of methods for spike sorting: the detection and classification of neural action potentials. *Network (Bristol, England)*, 9(4):R53–78.

Lozano, Y. R., Page, H., Jacob, P.-Y., Lomi, E., Street, J., and Jeffery, K. (2017). Retrosplenial and postsubicular head direction cells compared during visual landmark discrimination. *Brain Neurosci Adv*, 1.

Maguire, E. A. (2001). The retrosplenial contribution to human navigation: a review of lesion and neuroimaging findings. *Scand J Psychology*, 42(3):225–238.

Marchette, S. A., Vass, L. K., Ryan, J., and Epstein, R. A. (2014). Anchoring the neural compass: coding of local spatial reference frames in human medial parietal lobe. *Nat Neurosci*, 17(11):1598–1606.

Mathiasen, M. L., Dillingham, C. M., Kinnavane, L., Powell, A. L., and Aggleton, J. P. (2017). Asymmetric cross-hemispheric connections link the rat anterior thalamic nuclei with the cortex and hippocampal formation. *Neuroscience*, 349:128–143.

McCormick, D. A., Connors, B. W., Lighthall, J. W., and Prince, D. A. (1985). Comparative electrophysiology of pyramidal and sparsely spiny stellate neurons of the neocortex. *J Neurophys*, 54(4):782–806.

Meibach, R. C. and Siegel, A. (1977). Subicular projections to the posterior cingulate cortex in rats. *Exp Neurol*, 57(1):264–274.

Mitchell, A. S., Czajkowski, R., Zhang, N., Jeffery, K., and Nelson, A. J. D. (2018). Retrosplenial cortex and its role in spatial cognition. *Brain Neurosci Adv*, 2.

Mizuseki, K., Royer, S., Diba, K., and Buzsáki, G. (2012). Activity Dynamics and Behavioral Correlates of CA3 and CA1 Hippocampal Pyramidal Neurons. *Hippocampus*, 22(8):1659–1680.

Olvera-Cortés, E., Cervantes, M., and González-Burgos, I. (2002). Place-learning, but not cue-learning training, modifies the hippocampal theta rhythm in rats. *Brain Res Bull*, 58(3):261–270.

O'Mara, S. M. (2013). The anterior thalamus provides a subcortical circuit supporting memory and spatial navigation. *Front Syst Neurosci*, 7.

Opalka, A. N., Huang, W.-q., Liu, J., Liang, H., and Wang, D. V. (2020). Hippocampal Ripple Coordinates Retrosplenial Inhibitory Neurons during Slow-Wave Sleep. *Cell Rep*, 30(2):432–441.e3.

Page, H. J. I. and Jeffery, K. J. (2018). Landmark-Based Updating of the Head Direction System by Retrosplenial Cortex: A Computational Model. *Front Cell Neurosci*, 12.

Paxinos, G. and Watson, C. (2007). *The Rat Brain in Stereotaxic Coordinates: Hard Cover Edition*. Academic Press, Amsterdam; Boston, 6th edition

Pothuizen, H., Aggleton, J., and Vann, S. (2008). Do rats with retrosplenial cortex lesions lack direction? *Eur J Neurosci*, 28:2486–98.

Pothuizen, H., Davies, M., Albasser, M., Aggleton, J., and Vann, S. (2009). Granular and dysgranular retrosplenial cortices provide qualitatively different contributions to spatial working memory: Evidence from immediate-early gene imaging in rats. *Eur J Neurosci*, 30:877–88.

Pothuizen, H. H. J., Davies, M., Aggleton, J. P., and Vann, S. D. (2010). Effects of selective granular retrosplenial cortex lesions on spatial working memory in rats. *Behav Brain Res*, 208(2):566–575.

Powell, A., Connelly, W. M., Vasalauskaite, A., Nelson, A. J. D., Vann, S. D., Aggleton, J. P., Sengpiel, F., and Ranson, A. (2020). Stable Encoding of Visual Cues in the Mouse Retrosplenial Cortex. *Cereb Cortex*, 30(8):4424–4437.

Raji, C. A., Lopez, O. L., Kuller, L. H., Carmichael, O. T., and Becker, J. T. (2009). Age, Alzheimer disease, and brain structure. *Neurology*, 73(22):1899–1905.

Reed, J. M. and Squire, L. R. (1997). Impaired recognition memory in patients with lesions limited to the hippocampal formation. *Behav Neurosci*, 111(4):667–675.

Ruan, M., Young, C. K., and McNaughton, N. (2017). Bi-Directional Theta Modulation between the Septo-Hippocampal System and the Mammillary Area in Free-Moving Rats. *Front Neural Circuits*, 11.

Seki, M. and Zyo, K. (1984). Anterior thalamic afferents from the mamillary body and the limbic cortex in the rat. *J Comp Neurol*, 229(2):242–256

Sherrill, K. R., Erdem, U. M., Ross, R. S., Brown, T. I., Hasselmo, M. E., and Stern, C. E. (2013). Hippocampus and Retrosplenial Cortex Combine Path Integration Signals for Successful Navigation. *J Neurosci,* 33(49):19304–19313.

Shibata, H. (1992). Topographic organization of subcortical projections to the anterior thalamic nuclei in the rat. *J Comp Neurol*, 323(1):117–127.

Shibata, H. (1993). Efferent projections from the anterior thalamic nuclei to the cingulate cortex in the rat. *J Comp Neurol*, 330(4):533–542.

Shibata, H. (1994). Terminal distribution of projections from the retrosplenial area to the retrohippocampal region in the rat, as studied by anterograde transport of biotinylated dextran amine. *Neurosci Res*, 20(4):331–336.

Shibata, H., Honda, Y., Sasaki, H., and Naito, J. (2009). Organization of intrinsic connections of the retrosplenial cortex in the rat. *Anatomical Sci Internat*, 84(4):280.

Sripanidkulchai, K., & Wyss, J. M. (1986). Thalamic projections to retrosplenial cortex in the rat. *J Comp Neurol*, *254*(2), 143-165.

Sugar, J., Witter, M. P., van Strien, N. M., and Cappaert, N. L. M. (2011). The retrosplenial cortex: intrinsic connectivity and connections with the (para)hippocampal region in the rat. An interactive connectome. *Front Neuroinformatics*, 5:7.

Sutherland, R. J. and Hoesing, J. M. (1993). Posterior Cingulate Cortex and Spatial Memory: A Microlimnology Analysis. In Vogt, B. A. and Gabriel, M., editors, *Neurobiology of Cingulate Cortex and Limbic Thalamus: A Comprehensive Handbook*, pages 461–477. Birkhäuser, Boston, MA.

Szymusiak, R. and Nitz, D. (2003). Chronic recording of extracellular neuronal activity in behaving animals. *Curr Prot Neurosci*, Chapter 6: Unit 6.16.

Talk, A., Kang, E., and Gabriel, M. (2004). Independent generation of theta rhythm in the hippocampus and posterior cingulate cortex. *Brain Res*, 1015(1-2):15–24.

Taube, J. S. (1995). Head direction cells recorded in the anterior thalamic nuclei of freely moving rats. *J Neurosci*, 15(1 Pt 1):70–86.

Taube, J. S. (2007). The Head Direction Signal: Origins and Sensory-Motor Integration. *Ann Rev Neurosci*, 30(1):181–207. 10.1146/annurev.neuro.29.051605.112854.

Taylor, C. C. (2008). Automatic bandwidth selection for circular density estimation. *Computational Stat Data Analy*, 52(7):3493–3500.

Tsanov, M., Chah, E., Vann, S. D., Reilly, R. B., Erichsen, J. T., Aggleton, J. P., and O'Mara, S. M. (2011). Theta-Modulated Head Direction Cells in the Rat Anterior Thalamus. *J Neurosci*, 31(26):9489–9502.

1085 Tsanov, M., Chah, E., Wright, N., Vann, S. D., Reilly, R., Erichsen, J. T., Aggleton, J. P., and
1086 O'Mara, S. M. (2010). Oscillatory Entrainment of Thalamic Neurons by Theta Rhythm in
1087 Freely Moving Rats. *J Neurophys*, 105(1):4–17.

1088 Unal, G., Joshi, A., Viney, T. J., Kis, V., and Somogyi, P. (2015). Synaptic Targets of Medial
1089 Septal Projections in the Hippocampus and Extrahippocampal Cortices of the Mouse. *J*
1090 *Neurosci*, 35(48):15812–15826.

1091 van Groen, T. and Wyss, J. M. (1990). Connections of the retrosplenial granular a cortex in
1092 the rat. *J Comp Neurol*, 300(4):593–606.

1093 van Groen, T. and Wyss, J. M. (1990b). The postsubicular cortex in the rat: characterization
1094 of the fourth region of the subicular cortex and its connections. *Brain Res*, 529(1-2):165–
1095 177.

1096 van Groen, T. and Wyss, J. M. (1990c). The postsubicular cortex in the rat: characterization of
1097 the fourth region of the subicular cortex and its connections. *Brain Res*, 529(1-2):165–
1098 177.

1099 van Groen, T. and Wyss, J. M. (1992). Connections of the retrosplenial dysgranular cortex in
1100 the rat. *J Comp Neurol*, 315(2):200–216.

1101 Van Groen, T. and Wyss, J. M. (1995). Projections from the anterodorsal and anteroventral
1102 nucleus of the thalamus to the limbic cortex in the rat. *J Comp Neurol,* 358(4):584–604.

1103 Van Groen, T. and Wyss, J. M. (2003). Connections of the retrosplenial granular b cortex in
1104 the rat. *J Comp Neurol*, 463(3):249–263.

1105 Vann, S., Aggleton, J., and Maguire, E. (2009). What does the retrosplenial cortex do? *Nature*
1106 *Rev Neurosci*, 10:792–802.

1107 Vann, S. D. and Aggleton, J. P. (2002). Extensive cytotoxic lesions of the rat retrosplenial
1108 cortex reveal consistent deficits on tasks that tax allocentric spatial memory. *Behav*
1109 *Neurosci*, 116(1):85–94.

1110 Vann, S. D. and Aggleton, J. P. (2004). Testing the importance of the retrosplenial guidance
1111 system: effects of different sized retrosplenial cortex lesions on heading direction and
1112 spatial working memory. *Behav Brain Res*, 155(1):97–108.

1113 Vann, S. D. and Aggleton, J. P. (2005). Selective dysgranular retrosplenial cortex lesions in
1114 rats disrupt allocentric performance of the radial-arm maze task. *Behav Neurosci*,
1115 119(6):1682–1686.

1116 Vertes, R. P., Albo, Z., and Viana Di Prisco, G. (2001). Theta-rhythmically firing neurons in
1117 the anterior thalamus: implications for mnemonic functions of Papez's circuit.
1118 *Neuroscience*, 104(3):619–625.

1119 Vertes, R. P., Hoover, W. B., and Viana Di Prisco, G. (2004). Theta rhythm of the
1120 hippocampus: subcortical control and functional significance. *Behav Cog Neurosci Rev*,
1121 3(3):173–200.

1122 Vertes, R. P. and Kocsis, B. (1997). Brainstem-diencephalo-septohippocampal systems
1123 controlling the theta rhythm of the hippocampus. *Neuroscience*, 81(4):893–926.

1124 Vogt, B. A. and Miller, M. W. (1983). Cortical connections between rat cingulate cortex and
1125 visual, motor, and postsubicular cortices. *J Comp Neurol*, 216(2):192–210.

Whishaw, I. Q., Maaswinkel, H., Gonzalez, C. L., and Kolb, B. (2001). Deficits in allothetic and idiothetic spatial behavior in rats with posterior cingulate cortex lesions. *Behav Brain Res*, 118(1):67–76.

Witter, M. P., Ostendorf, R. H., and Groenewegen, H. J. (1990). Heterogeneity in the Dorsal Subiculum of the Rat. Distinct Neuronal Zones Project to Different Cortical and Subcortical Targets. *Eur J Neurosci*, 2(8):718–725.

Yamawaki, N., Li, X., Lambot, L., Ren, L. Y., Radulovic, J., and Shepherd, G. M. G. (2019). Long-range inhibitory intersection of a retrosplenial thalamocortical circuit by apical tuft-targeting CA1 neurons. *Nat Neurosci*, 22(4):618–626.

Yoder, R. M. and Taube, J. S. (2014). The vestibular contribution to the head direction signal and navigation. *Front Integrative Neurosci*, 8.

Young, C. K. and McNaughton, N. (2009). Coupling of theta oscillations between anterior and posterior midline cortex and with the hippocampus in freely behaving rats. *Cereb Cortex*, 19(1):24–40.

Zakowski, W., Zawistowski, P., Braszka, u., and Jurkowlaniec, E. (2017). The effect of pharmacological inactivation of the mammillary body and anterior thalamic nuclei on hippocampal theta rhythm in urethane-anesthetized rats. *Neuroscience*, 362:196–220.

Web references

Waveform Analysis (MATLAB / GNU Octave) toolbox. Original publication and links to open source Git repository:

- Ardid, S., Vinck, M., Kaping, D., Marquez, S., Everling, S., and Womelsdorf, T. (2015). Mapping of Functionally Characterized Cell Classes onto Canonical Circuit Operations in Primate Prefrontal Cortex. *J Neurosci*, 35(7):2975–2991.

- https://bitbucket.org/sardid/waveformanalysis, Salva Ardid PhD. Last accessed: 15/06/2021.